Modelling vortex-induced vibrations of branched structures by coupling a 3D-corotational frame finite element formulation with wake-oscillators

Alexandre Villié[1*], Mauricio C. Vanzulli[2], Jorge M. Pérez Zerpa[3], Jérôme Vétel[1], Stéphane Etienne[1], Frédérick P. Gosselin[1]

[1]*Département de génie mécanique, Polytechnique Montréal, Montréal, Canada*

[2]*Instituto de Ingeniería Mecánica y Producción Industrial, Facultad de Ingeniería, Universidad de la República, Montevideo, Uruguay*

[3]*Instituto de Estructuras y Transporte, Facultad de Ingeniería, Universidad de la República, Montevideo, Uruguay*

[*]*Corresponding Author: alexandre.villie@polymtl.ca*

Abstract

Branched structures are present in a diverse set of problems, from modelling branch pipe connections to simulating tree dynamics. Soft corals like the Bipinnate sea plume, have a branched geometry and are soft enough to bend under the waves. Due to their cylindrical cross section, a vortex street forms in the coral's wake inducing vibrations of its branches. Despite extensive studies on VIV in straight geometries, the three-dimensional (3D) dynamics of flexible branched structures remains uninvestigated. In this numerical and experimental study, we develop a novel formulation for the accurate computation of in-line and cross-flow VIV of frame structures undergoing large deformation. The finite element approach is used to model arbitrarily complex geometries of branched frame structures. Our formulation allows to model complex geometries with forks or sharp angles. The consistent 3D corotational formulation for frame elements computes the internal, inertial and hydrodynamic forces. A wake-oscillator approach models the near wake dynamics with fluctuating fluid forces on the structure in the in-line and cross-flow directions. The drag and lift coefficients follow distributed Van der Pol oscillators. Moreover, we implement the numerical resolution procedure in the open-source library ONSAS. The present formulation and numerical resolution procedure is validated by solving three examples, including comparisons with an analytical solution, a wake-oscillator, and experimental data from the literature. We also conduct experiments of a flexible and elastic cylinder clamped inside a water tunnel under a constant uniform flow. Amplitudes and power spectral density of the tip transverse displacements are compared with the model prediction. Finally, the proposed formulation is applied on a cylinder with two branches. The simulations demonstrate a multi-frequency response with higher amplitudes of displacements when additional branches are incorporated onto the cylinder, emphasizing the significance of considering VIV in nature and engineering applications for such geometries.

Keywords: Vortex-induced vibrations, Wake-oscillator, Corotational framework, Biomechanics

1. Introduction

Vortex-Induced Vibrations (VIV) are widely studied in engineering to mitigate offshore structure oscillations [7, 50, 20, 47], for vibrations control [35, 13] and more recently as a potential source of clean energy [5, 71, 23].

VIV are characterized by a coupling between the vibration s of a structure and the flow fluctuations in its wake. An asymmetric vortex shedding exerts oscillating drag and lift forces, inducing in-line and cross-flow vibrations [57, 34].

Marine life has developed mechanisms through evolution to cope with VIV. These adaptations are observed across various organisms and serve different purposes. For example, some plants benefit from flow-induced vibrations, which enhance the dispersion rate of underwater plant canopies [58] or facilitate pollination [45]. A seal's whiskers structural design mitigates flow-induced vibrations to better chase preys in the dark [29, 4, 43]. On the other hand, some animals use VIV to increase pheromone capture for moth males [61] or heat exchange for coral tentacles [44]. In the context of soft corals, Gosselin first reported VIV on the flexible branches of *Antillogorgia bipinnata*. Two-dimensional (2D) simulations of a vibrating cross section conducted in Ref.[10] demonstrate an increase in particle capture of up to 40 % more than a fixed branch during lock-in, suggesting that sea plumes may use VIV as a feeding strategy.

Incorporating VIV into biomechanical models of plant is necessary to improve the accuracy and realism of computational simulations. Numerous studies have highlighted the importance of accounting for flexibility when modeling the behavior of plants submitted to hydrodynamic forces [42, 39, 63]. Experimental studies [11, 65] and numerical simulations [70, 38] show that continuous flexible structures encounter multiple lock-ins due to the multiplicity of their natural frequencies. The intricate interplay between nonlinear wake dynamics and multi-modal response presents significant challenges for modeling VIV in flexible structures and requires special numerical tools.

One approach to study VIV numerically is to solve a fully coupled system with the Navier Stokes equations for the fluid and the elastodynamics equations for the structure. Several numerical methods in Computational Fluid Dynamics (CFD) have been used to predict VIV, such as Quasi-three-dimensional Method [69], coupled three-dimensional (3D) Finite Element Method (FEM) [31] or Finite Volume Method [46]. However, simulating all of the surrounding fluid flow is extremely computationally demanding due to the vast range of length and time scales and to the large amplitudes of motion that must be considered.

One alternative method is to empirically model the forcing of the wake on the structure. Bishop and Hassan and Hartlen and Currie proposed the wake-oscillator model (WOM) to simulate the hydrodynamic forcing of the wake on a rigid cylinder. Facchinetti et al. set a phenomenological coupling between the cross section acceleration and the wake variable. Violette et al. showed that coupling the dynamics of a flexible cylinder with the nonlinear Van der Pol oscillator exhibits good agreements with Direct numerical simulation (DNS) results.

Aquatic plants and soft corals are flexible and interact with the flow developing large deflections [27, 16, 17]. Jain and Modarres-Sadeghi experimentally observed a vortex shedding parallel to the cylinder's axis for inclination angles up to 65°. They validate the independence principle, stating that the inclined cylinders can be treated as the normal-incidence ones by considering only the component of the free stream velocity normal to the cylinder axis. With a finite element approach, the independence principle allows for the straightforward extension of the WOM to inclined structures. Prior works implementing a FEM formulation of the WOM [38, 68, 40] as well as commercial codes [41] have consistently defined the wake variables as additional degrees of freedom assigned to each node. However, these studies primarily focused on analyzing structures with straight geometries, neglecting the presence of forks, angles, or other complex geometric features. Consequently, the issue of having discontinuous tangent vectors at specific nodes, which can result in ill-defined cross-flow directions, has not been addressed in these prior investigations. Numerous wind-tree numerical models have been developed [59, 32, 55, 56, 18] and various simulations of tree dynamics have been performed [1, 28, 53]. However, these studies often overlook VIV. The assessment of VIV on 3D branched structures like corals or trees undergoing large displacements remains an open problem. The motivation of this study is to develop a novel methodology for incorporating VIV in 3D simulations of branched structures, using the WOM.

Structures undergoing VIV are typically slender and can exhibit large amplitude beam-like deformations. The kinematics of a flexible frame element can be described by the total Lagrangian or the updated Lagrangian formulations, however they require a high number of elements or a small time step in order to provide proper results for nonlinear problems [19, 37]. Crisfield et al. presented a 3D corotational formulation in which the movement is separated into two parts using an element-independent framework. The first part involves rigid body motion, which includes translation and rotation from the global to the rigid system. The second part involves a small deformation motion, which goes from the rigid to the deformed configuration. This formulation handles large rotations and large displacements, obtaining accurate results with a smaller number of elements [37]. The corotational model has been gradually extended to consider warping effects [3], dynamic problems [36], a consistent formulation for frame elements [37] and hydrodynamic forces [66]. Corotational frame elements have been used in fluid-structure interaction simulations to model living organisms subjected to fluid loads, such as insect wings during flapping [14], or vibrating vocal folds [64].

Here we present a unified corotational formulation for simulating branched frame structures undergoing large displacements and rotations, coupled with a the wake-oscillator model to assess VIV. The consistent 3D corotational frame element formulation computes the internal, inertial and hydrodynamic forces. Moreover, we implement the formulation in the open-source structural analysis tool ONSAS[1] [51] and experiments are performed for validation. As a result, a new free tool for VIV analysis of 3D forked structures is available.

The paper is structured as follows: in Section 2 we present the formulation of the in-line/cross-flow wake-oscillator model in the 3D corotational framework together with the experimental setup. In Section 3 the in-line and cross-flow VIV model is verified with one frame element (Example 1). The model is validated in large displacements

[1] `www.onsas.org`

with the wake-oscillator model from Leclercq and de Langre (Example 2) and with experimental data from Trim et al. (Example 3). It is also compared with new experimental data in Example 4. Simulation results of VIV on a forked structure are presented in Example 5. The paper ends with the conclusions in Section 4.

2. Methodology

In this section, we introduce our proposed corotational formulation for the WOM and added mass, along with a numerical procedure for solving the governing equations. Additionally, we provide a detailed description of the experimental setup used to validate our model.

The formulation is developed for a frame element with a length l_0 and a circular, uniform cross section of diameter D and second moment of inertia I. The material is considered to be elastic and isotropic, of density ρ and elasticity modulus E. In this section, extensions of the corotational formulation are developed and a numerical resolution procedure is presented.

1. Corotational framework

We summarize here the key steps of the corotational formulation from [37]. The 3D corotational framework uses three coordinate systems. The global reference system is defined by the triad $(\mathbf{e}_\mathrm{x}, \mathbf{e}_\mathrm{y}, \mathbf{e}_\mathrm{z})$. The local system attached to the element after a rigid rotation without deformation is $(\mathbf{r}_1, \mathbf{r}_2, \mathbf{r}_3)$. The triad that is rigidly attached to each node is $(\mathbf{t}_1, \mathbf{t}_2, \mathbf{t}_3)$. These coordinates systems are illustrated in Fig. 1.

Let us consider a two-node frame element, where the nodal displacements are represented by the column vector $\mathbf{d} = \left[(\mathbf{u}^1)^T, (\mathbf{w}^1)^T, (\mathbf{u}^2)^T, (\mathbf{w}^2)^T\right]^T$. Here, $\mathbf{u}^i$ and $\mathbf{w}^i$ denote the column vectors of linear displacements and rotations, respectively, at node i. These displacements can be expressed in both the global coordinate system as $\mathbf{d}_g$ and the local coordinate system as $\mathbf{d}_l$. Similarly, a vector of nodal forces $\mathbf{f}$ can also be represented in the corresponding coordinate systems.

The internal force $\mathbf{f}_{int}$ is derived based on the work of Ref.[3]. This forces vector is expressed in the local coordinates system where the Euler-Bernoulli beam theory is assumed. Translations and rotations at the cross section centroid are interpolated from the local nodal values, using linear shape functions for the axial displacement and rotation, and cubic shape functions for transverse displacements.

The internal virtual work is the same in local and global coordinates, therefore:

$$\delta\mathbf{d}_g^T \mathbf{f}_{int,g} = \delta\mathbf{d}_l^T \mathbf{f}_{int,l}, \tag{1}$$

with $\delta\mathbf{d}_g$ and $\delta\mathbf{d}_l$ being the virtual displacements in global and local coordinates, respectively. We can express

$$\delta\mathbf{d}_l = \mathbf{B}\delta\mathbf{d}_g, \tag{2}$$

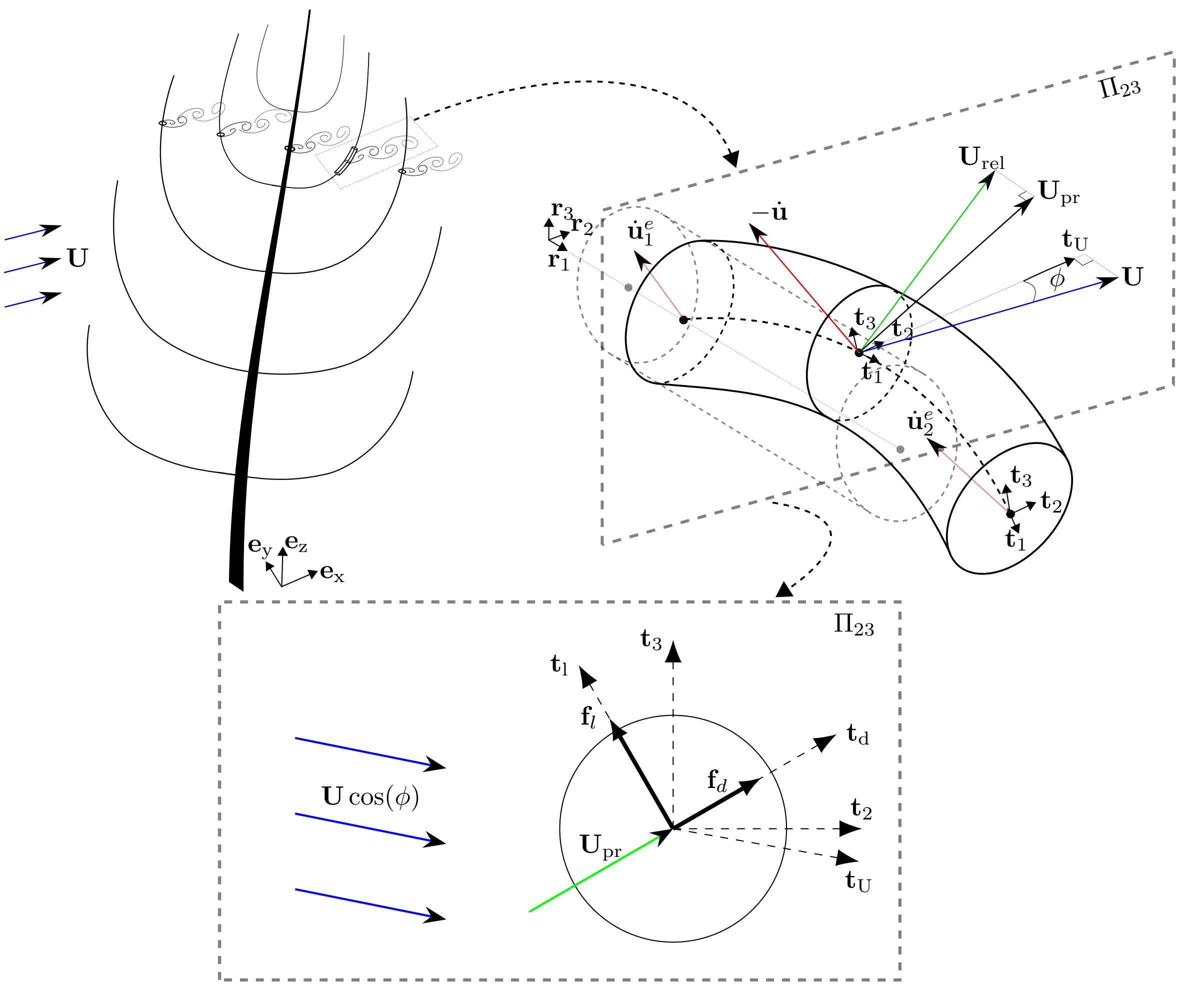

Figure 1: 3D an planar illustration of corotational kinematics and hydrodynamics forces.

with $\mathbf{B}$ being a transformation matrix expressing the axial displacements and rotations from the local to the global coordinate system. It follows

$$\delta \mathbf{d}_g^T \mathbf{f}_{int,g} = \delta \mathbf{d}_g^T \mathbf{B}^T \mathbf{f}_{int,l}. \tag{3}$$

This is valid for any virtual displacement $\delta \mathbf{d}_g$, so:

$$\mathbf{f}_{int,g} = \mathbf{B}^T \mathbf{f}_{int,l}, \tag{4}$$

where $\mathbf{f}_{int,l} = \left[f_{a\ell} \ \ (\mathbf{m}_\ell^1)^T \ (\mathbf{m}_\ell^2)^T \right]$ is the vector of internal forces in local coordinates. It considers the axial force $f_{a\ell}$ along $\mathbf{t}_1$, bending moments and torsional moment $\mathbf{m}_\ell^i$ at node i along $\mathbf{t}_1$ and $\mathbf{t}_2, \mathbf{t}_3$, respectively. They are given by a linear constitutive behavior.

The inertial force is obtained through the kinetic energy variations. The kinetic energy K of the element is:

$$K = \frac{1}{2} \int_{l_0} \rho \dot{\mathbf{u}}^T A \dot{\mathbf{u}} + \rho \dot{\mathbf{w}}^T \mathbf{I} \dot{\mathbf{w}} \ dl, \tag{5}$$

with $\mathbf{u}, \mathbf{w}$ being the displacements and rotations vectors of the center of the cross section, A the cross section area and $\mathbf{I}$ the geometric inertia tensor. The dot notation stands for time differentiation. Using the derivative chain rule, the variations of Eq. (5) writes:

$$\delta K = - \int_{l_0} \delta \mathbf{u}^T \rho A \ddot{\mathbf{u}} + \delta \mathbf{w}^T [\rho \mathbf{I} \ddot{\mathbf{w}} + \widetilde{\dot{\mathbf{w}}} \rho \mathbf{I} \dot{\mathbf{w}}] \ dl, \tag{6}$$

with $\widetilde{\dot{\mathbf{w}}}$ being the skew operator associated to the vector $\dot{\mathbf{w}}$. The inertial force vector of the element in global coordinates is:

$$\delta K = (\mathbf{f}_{\text{ine}})^T \delta \mathbf{d}_g, \tag{7}$$

where

$$\mathbf{f}_{\text{ine}} = \int_{l_0} \left\{ \mathbf{H}_1^T \mathbf{R}_r^T \rho A \ddot{\mathbf{u}} + \mathbf{H}_2^T \mathbf{R}_r^T [\rho \mathbf{I} \ddot{\mathbf{w}} + \widetilde{\dot{\mathbf{w}}} \rho \mathbf{I} \dot{\mathbf{w}}] \right\} \ dl. \tag{8}$$

The rigid rotation matrix $\mathbf{R}_r$ expresses $(\mathbf{r}_1, \mathbf{r}_2, \mathbf{r}_3)$ in the global coordinate system. Matrices $\mathbf{H}_1, \mathbf{H}_2$ depend on the interpolation functions which are linear for axial displacements and hermitian for bending. Their exact expression can be found in Ref.[37].

2. Hydrodynamic forces

The structure is submitted to a uniform and steady flow of velocity $\mathbf{U}$ and density ρ_{f}. The hydrodynamic forces acting on the structure are the added mass, the steady drag, and the fluctuating drag and lift forces due to the shed vortices. We define the instantaneous relative velocity $\mathbf{U}_{\text{rel}}$ that the cylinder perceives based on $\mathbf{U}$ and the cylinder velocity $\dot{\mathbf{u}}$: $\mathbf{U}_{\text{rel}} = \mathbf{U} - \dot{\mathbf{u}}$. In this formulation, the computation of the fluid forces is performed at every instant in each section plane by considering only the normal component of the flow velocity, as stated by the independence principle. Thus, the relative velocity is projected on the cross section plane Π_{23} as shown in Fig. 1. This projection is denoted $\mathbf{U}_{\rm pr}$. We define the vector $\mathbf{t}_{\rm U}$ as the normalized projection of $\mathbf{U}$ on the cross section plane in local coordinates:

$$\mathbf{t}_{\rm U} = \mathbf{L}_2 \left(\mathbf{R}_{\rm r}\overline{\mathbf{R}}\right)^T \mathbf{U}/\|\mathbf{L}_2 \left(\mathbf{R}_{\rm r}\overline{\mathbf{R}}\right)^T \mathbf{U}\|, \tag{9}$$

with $\left(\mathbf{R}_r\overline{\mathbf{R}}\right)^T$ being the rotation matrix used to transform a global vector into local coordinates. The operator $\mathbf{L}_2$ projects it onto the section plane Π_{23}. $\mathbf{t}_{\rm U}$ provides the flow direction seen by the cross section. The fluid velocity in the cross section plane is $\mathbf{U} - \mathbf{U}\cdot\mathbf{t}_1 = U\cos(\phi)\mathbf{t}_{\rm U}$, with ϕ being the angle between the fluid velocity $\mathbf{U}$ and Π_{23}. A 3D and planar representation of these vectors and angles is provided in Fig. 1. The added mass force per unit length acting on the section is:

$$\mathbf{f}_a(s,t) = m_{\rm a}\left(\dot{\mathbf{U}}(s,t) - \ddot{\mathbf{u}}(s,t)\right), \tag{10}$$

with $m_{\rm a} = C_a\rho_{\rm f}D\pi/4$ being the fluid added mass. The added mass coefficient C_a is assumed to be 1 for a circular cross section [8]. Here, the flow is considered as steady: $\dot{\mathbf{U}} = 0$. The corotational formulation of the added mass force acting on a beam element of length l_0 is expressed as an inertial force of the same element having a density $C_a\rho_{\rm f}$:

$$\mathbf{f}_{am} = -\int_{l_0}\left\{\mathbf{H}_1^T\mathbf{R}_{\rm r}^T C_a\rho_{\rm f}A\ddot{\mathbf{u}} + \mathbf{H}_2^T\mathbf{R}_{\rm r}^T[C_a\rho_{\rm f}\mathbf{I}\ddot{\mathbf{w}} + \widetilde{\dot{\mathbf{w}}}C_a\rho_{\rm f}\mathbf{I}\dot{\mathbf{w}}]\right\}dl. \tag{11}$$

At time t and curvilinear coordinate s, the instantaneous drag and lift forces per unit length are:

$$\mathbf{f}_{\rm drag}(s,t) = \frac{1}{2}C_D(s,t)\rho_{\rm f}DU_{\rm pr}^2(s,t)\mathbf{t}_d(s,t), \tag{12}$$

$$\mathbf{f}_{\rm lift}(s,t) = \frac{1}{2}C_L(s,t)\rho_{\rm f}DU_{\rm pr}^2(s,t)\mathbf{t}_l(s,t), \tag{13}$$

with $\mathbf{t}_d, \mathbf{t}_l$ being the drag and lift directions, respectively. These forces are derived from the empirical WOM that models the fluctuating pressure field on the cylinder caused by vortices in its wake by oscillating drag and lift coefficients C_D and C_L. In particular, the in-line vibrations are modeled by splitting the instantaneous drag coefficient $C_D = C_D^0 + C_{Di}$ into a constant mean coefficient C_D^0 and a fluctuating component induced by the wake C_{Di}^0 following [26, 68, 40, 25]. The instantaneous vortex-induced drag and lift coefficients are modeled by

$$C_{Di}(s,t) = \frac{1}{2}C_{Di}^0 p(s,t), \tag{14}$$

$$C_L(s,t) = \frac{1}{2}C_L^0 q(s,t), \tag{15}$$

with C_{Di}^0, C_L^0 being the constant amplitudes of the fluctuating drag and lift coefficients on a stationary cylinder. The variables p and q are the dimenionless in-line and cross-flow wake variables. They can be seen as the normalized drag and lift coefficients. They both follow nonlinear Van der Pol oscillators and are coupled to the section acceleration:

$$\ddot{p}(s,t) + 2\epsilon_p\Omega_f\left(p^2(s,t)-1\right)\dot{p}(s,t) + 4\Omega_f^2 p(s,t) = \frac{A_p}{D}\ddot{u}_p(s,t), \tag{16}$$

$$\ddot{q}(s,t) + \epsilon_q\Omega_f\left(q^2(s,t)-1\right)\dot{q}(s,t) + \Omega_f^2 q(s,t) = \frac{A_q}{D}\ddot{u}_q(s,t), \tag{17}$$

where $\Omega_f = 2\pi S_t U\cos\phi/D$ is the wake angular frequency, A_p, A_q are the coupling coefficients, ϵ_p, ϵ_q are the fluid damping parameters, S_t is the Strouhal number and $\ddot{u}_p, \ddot{u}_q$ are the in-line and cross-flow accelerations, respectively. For any cross-section in a frame element, $\ddot{u}_p, \ddot{u}_q$ are defined as:

$$\ddot{u}_p = \ddot{\mathbf{u}}\cdot\mathbf{t}_{\mathrm{U}}, \tag{18}$$

$$\ddot{u}_q = \ddot{\mathbf{u}}\cdot(\mathbf{t}_1\times\mathbf{t}_{\mathrm{U}}). \tag{19}$$

At a bifurcation or branch node, both $\mathbf{t}_1$ and $\mathbf{t}_{\mathrm{U}}$ are discontinuous. Therefore, $\ddot{u}_p$ and $\ddot{u}_q$ at this node are ill-defined. To avoid this issue, we set the wake variables as uniform on each element where $\mathbf{t}_1$ and $\mathbf{t}_{\mathrm{U}}$ remain continuous. Therefore, the Van der Pol oscillator is solved once per element. This novel approach enables the application of the WOM to interconnected frame elements, accommodating arbitrary connections such as forks and sharp angles.

For both in-line and cross-flow oscillators, the coupling is done by averaging the two nodal accelerations of the element:

$$\ddot{p} + 2\epsilon_p\Omega_f\left(p^2-1\right)\dot{p} + 4\Omega_f^2 p = \frac{A_p}{D}\left(\ddot{u}_p^1+\ddot{u}_p^2\right)/2, \tag{20}$$

$$\ddot{q} + \epsilon_q\Omega_f\left(q^2-1\right)\dot{q} + \Omega_f^2 q = \frac{A_q}{D}\left(\ddot{u}_q^1+\ddot{u}_q^2\right)/2, \tag{21}$$

where the subscripts $\cdot_p$ and $\cdot_q$ denote the in-line and cross-flow directions, respectively, and the superscripts $\cdot^1$ and $\cdot^2$ refer to the element nodes. The cross product $\mathbf{t}_1\times\mathbf{t}_{\mathrm{U}}$ provides the cross-flow direction. $\ddot{\mathbf{u}}\cdot\mathbf{t}_{\mathrm{U}}$ and $\ddot{\mathbf{u}}\cdot(\mathbf{t}_1\times\mathbf{t}_{\mathrm{U}})$ are the accelerations of the cross section in the in-line and cross-flow directions. Eqs (16,17) are known to provide quasi-harmonic oscillations of normalized amplitude $P^0 = 2$, $Q^0 = 2$ for $\Omega_f = 1$. As the WOM is a phenomenological model, these coefficients $S_t, A_p, A_q, \epsilon_p, \epsilon_q$ are calibrated with experimental data.

The corotational formulation of the drag and lift force acting on one element is taken from Ref.[66]:

$$\mathbf{f}_d = \frac{1}{2}\rho_{\mathrm{f}}D\mathbf{E}\int_{l_0}\left\{\mathbf{H}_1^T\overline{\mathbf{R}}\|\mathbf{L}_2\left(\mathbf{R}_r\overline{\mathbf{R}}\right)^T\mathbf{U}_{\mathrm{rel}}\|C_D(p)\mathbf{L}_2\left(\mathbf{R}_r\overline{\mathbf{R}}\right)^T\mathbf{U}_{\mathrm{rel}}\right\}dl, \tag{22}$$

$$\mathbf{f}_l = \frac{1}{2}\rho_{\mathrm{f}}D\mathbf{E}\int_{l_0}\left\{\mathbf{H}_1^T\overline{\mathbf{R}}\|\mathbf{L}_2\left(\mathbf{R}_r\overline{\mathbf{R}}\right)^T\mathbf{U}_{\mathrm{rel}}\|C_L(q)\mathbf{L}_3\mathbf{L}_2\left(\mathbf{R}_r\overline{\mathbf{R}}\right)^T\mathbf{U}_{\mathrm{rel}}\right\}dl. \tag{23}$$

where the operator $\mathbf{L}_3 = \exp([\pi/2,0,0]^T)$ rotates the relative fluid velocity by $\pi/2$ radians around the axis $\mathbf{t}_1$ to provide the local lift direction. Finally, $\overline{\mathbf{R}}$ and $\mathbf{E}$ transform the velocity from local to rigid and from rigid to global coordinates, respectively [3, 66].

Note that the fluid damping is included in the drag force. Indeed, as pointed out by Ogink and Metrikine, a linearized form of the instantaneous drag force can lead to a fluid damping term proportional to the section velocity, named stall term by Skop and Balasubramanian, Facchinetti et al.. In the 2D VIV, this hypothesis may not be respected. Here, we consider the full nonlinear drag force following [48, 52].

When attempting to solve for the dynamics of a branched structure, a system of differential equations needs to be solved for each branch, and continuity conditions must be imposed at the bifurcation nodes, which results in a significant increase in the complexity of the problem. In the proposed formulation, the FEM assembly approach is considered. Therefore, no complexity is added by including a fork node in the structure.

3. *Balance equations and numerical resolution procedure*

The governing equations are derived by applying the principle of virtual work to all elements of the structure for the forces described in Eqs.(8), (11), (23), and (22), while simultaneously solving the Van der Pol equations, Eqs.(20) and (21), for each element.

We denote the structure assembled vectors with subscripts $\cdot_s$ and elements variables with superscripts $\cdot^e$. The solid and wake residuals are:

$$\begin{cases} \mathbf{r}_u = \mathbf{f}_{int,s}(\mathbf{d}_s) + \mathbf{f}_{ine,s}(\mathbf{d}_s, \dot{\mathbf{d}}_s, \ddot{\mathbf{d}}_s) - \mathbf{f}_{am,s}(\ddot{\mathbf{d}}_s) - \mathbf{f}_{d,s}(\mathbf{d}_s, \dot{\mathbf{d}}_s, \mathbf{p}_s) - \mathbf{f}_{l,s}(\mathbf{d}_s, \dot{\mathbf{d}}_s, \mathbf{q}_s), & \\ r_p^e = \ddot{p}^e + 2\epsilon_p \Omega_f \left(p^{e^2} - 1 \right) \dot{p}^e + 4\Omega_f^2 p^e - \frac{A_p}{D} \left(\ddot{u}_p^{e,1} + \ddot{u}_p^{e,2} \right)/2, & e = 1, \dots, N_e \\ r_q^e = \ddot{q}^e + \epsilon_p \Omega_f \left(q^{e^2} - 1 \right) \dot{q}^e + \Omega_f^2 q^e - \frac{A_q}{D} \left(\ddot{u}_q^{e,1} + \ddot{u}_q^{e,2} \right)/2, & \end{cases} \tag{24}$$

where $\mathbf{r}_u$ is the residual of the Principle of Virtual Work equations, and the wake residuals r_p^e, r_q^e correspond to the Van der Pol equations. They are both computed independently for each element. For each time step, the system $\mathbf{r}_u = \mathbf{0}; r_p = r_q = 0$ must be solved, obtaining the current configuration of the structure (with velocities and accelerations) and wake variables for each element.

We define the following non-dimensional parameters: the reduced velocity, the Reynolds number, the aspect ratio and the mass ratio, respectively,

$$U_R = \frac{U}{D\ell^2}\sqrt{\frac{m_\mathrm{s} + m_\mathrm{a}}{EI}}, \quad R_\mathrm{e} = \frac{UD}{\nu_\mathrm{f}}, \quad \Gamma = \frac{\ell}{D}, \quad \mathcal{M} = \frac{\rho}{\rho_\mathrm{f}}, \tag{25}$$

with m_s being the structural mass per unit length and ν_f the fluid kinematic viscosity.

The system of nonlinear governing Eq. (24) is solved numerically using iterative methods. The internal forces are implemented according to the formulations described in [37, 3]. The inertial forces in Eq. (8) and hydrodynamic forces in Eqs (11, 23, 22) are computed with 4 Gauss integration points. The tangent matrices of the hydrodynamic forces are considered for large displacement examples as recommended in Ref. [66]. The trapezoidal Newmark numerical method is used to solve the dynamic problem Eq. (24) with $\alpha = 1/4$, $\delta = 1/2$ [2].

To solve for r_p and r_q in Eq. (24), a fourth-order Runge-Kutta algorithm (implemented using the `ode45` function in Matlab) solves the nonlinear Van der Pol equations Eqs (16), 17) with constant nodal accelerations $\ddot{\mathbf{u}}^1$, $\ddot{\mathbf{u}}^2$ at each Newton iteration. The wake variables (p, q) are defined as uniform in the element. In all of the examples, two stopping criteria are considered based on either the norm of the relative displacement, $||\Delta\mathbf{u}||/\mathbf{u} < \text{tol}_u$, or the norm of the residual force, $r_u < \text{tol}_r$. Both criteria are used to determine convergence of the numerical solution. Algorithms 1 and 2 describe the iterative procedure for resolution.

For non-homogeneous initial configurations, the numerical method is initialized with a given deformed configuration and initial velocities and accelerations. To start from the steady state, the Newton-Raphson method solves the static problem and obtain the initial configuration.

Algorithm 1 Numerical procedure

Initialize the structure $u_t \leftarrow u_0,\ \ \dot{u}_t \leftarrow \dot{u}_0,\ \ddot{u}_t \leftarrow \ddot{u}_0$
Initialize the wake $(p^{k+1}, \dot{p}^{k+1}, q^k, \dot{q}^{k+1}) \leftarrow (p_0, \dot{p}_0, q_0, \dot{q}_0)$
while $t < t_f$ **do**
    Initial guess for $t + \Delta t$: $\ (\mathbf{u}^k, \dot{\mathbf{u}}^k, \ddot{\mathbf{u}}^k) \leftarrow (\mathbf{u}_t, \dot{\mathbf{u}}_t, \ddot{\mathbf{u}}_t)$
    Compute $\mathbf{r}_u^{k+1}$ and assemble the tangent matrix
    while $\|\Delta\mathbf{u}^{k+1}\| > \text{tol}_u\ \ \&\ \ \|\mathbf{r}_u^{k+1}\| > \text{tol}_r\ \ \&\ \ k < \text{max}_{iter}$ **do**
        Compute $\Delta\mathbf{u}^{k+1}$
        Update $\mathbf{u}^{k+1} \leftarrow \mathbf{u}^k + \Delta\mathbf{u}^{k+1}$
        Newmark method gives next candidates $\dot{\mathbf{u}}^{k+1}, \ddot{\mathbf{u}}^{k+1}$
        Algorithm 2 computes wake variables: $p^{k+1}(\ddot{\mathbf{u}}^{k+1})$, $q^{k+1}(\ddot{\mathbf{u}}^{k+1})$
        Update $\mathbf{f}_{int,s}^{k+1}(\mathbf{u}^{k+1})$, $\mathbf{f}_{ine,s}^{k+1}(\mathbf{u}^{k+1}, \dot{\mathbf{u}}^{k+1}, \ddot{\mathbf{u}}^{k+1})$, $\mathbf{f}_{flu,s}^{k+1}(\mathbf{u}^{k+1}, \dot{\mathbf{u}}^{k+1}, p^{k+1}, q^{k+1})$
        Compute $\mathbf{r}_u^{k+1}(\mathbf{u}^{k+1}, \dot{\mathbf{u}}^{k+1}, \ddot{\mathbf{u}}^{k+1})$ and assemble the tangent matrix
    end while
    $(\mathbf{u}_{t+\Delta t}, \dot{\mathbf{u}}_{t+\Delta t}, \ddot{\mathbf{u}}_{t+\Delta t}, p_{t+\Delta t}, q_{t+\Delta t}) \leftarrow (\mathbf{u}^{k+1}, \dot{\mathbf{u}}^{k+1}, \ddot{\mathbf{u}}^{k+1}, p^{k+1}, q^{k+1})$
    $t \leftarrow t + \Delta t$
end while

Algorithm 2 Wake equations resolution

Returns Wake variables candidates p^{k+1}, q^{k+1} of the element for time $t + \Delta t$
Initial guess $(p^{k+1}, \dot{p}^{k+1}, q^k, \dot{q}^{k+1}) \leftarrow (p_t, \dot{p}_t, q_t, \dot{q}_t)$
Compute averaged element in-line and cross-flow accelerations $\ddot{\mathbf{u}}_p^{k+1}, \ddot{\mathbf{u}}_q^{k+1}$ using Eqs (18, 19)
Compute $r_p(p^{k+1}, \dot{p}^{k+1}, \ddot{\mathbf{u}}_p^{k+1})$ and $r_q(q^k, \dot{q}^{k+1}, \ddot{\mathbf{u}}_q^{k+1})$ using Eqs (20,21)
`ode45` solves $r_p = 0$
`ode45` solves $r_q = 0$
$(p^{k+1}, \dot{p}^{k+1}) \leftarrow (p_{ode}, \dot{p}_{ode})$
$(q^k, \dot{q}^{k+1}) \leftarrow (q_{ode}, \dot{q}_{ode})$

4. *Experimental methodology*

In order to validate the numerical model, we carry experimental measurements of cross-flow VIV. The elongated cylinder is 3D printed with Selective Laser Sintering using a Sinterit Lisa Pro printer. The printed material is Thermoplastic Elastomer (TPE powder) known for its elasticity and flexibility. The cylinder is $\ell = 150$ mm in height,

Figure 2: Experimental setup for $U = 0.56$ m/s ($U_R = 20$). Flow direction is from left to right.

which is the maximum height achievable by the printer. We selected a circular cross section with a diameter of $D = 5$ mm. This choice strikes a balance between having a high slenderness ($\Gamma = 30$) and achieving a satisfactory surface resolution. Since the material is porous, its density $\rho = 7.9 \times 10^2$ kg/m^3 is calculated by dividing its wet weight by its volume (given in the design software). A three-points bending test provides the bending rigidity of the structure $EI = 4 \times 10^2$ N mm^2.

The structure is placed in a closed water tunnel, which is operated by two pumps. The main pump allows for flow velocities ranging from 0.13 m/s to 9 m/s, while the secondary pump is used to achieve flow velocities below 0.18 m/s. One flow meter measures the flow rate for each pump, which is then converted to a mean flow velocity in the test section. The test section area is 250×250 mm^2. The bottom end of the cylinder is clamped by screwing an M5 hexagonal nut which is embedded to the support plate. The quantities of interest are the amplitude and frequency of the transverse displacements at the tip of the cylinder as they vary with the reduced velocity. The flow velocity U is varied in steps, and for each step, we wait 30 seconds for the steady-state regime to be established. Then, a Go Pro Hero Black 12 records a 4K-quality movie for 20 seconds (~ 100 periods) of the transverse displacements at a frame rate of 120 frames per second. The camera is positioned 340 mm downstream from the structure (Fig. 2). This distance is large enough not to interact with the wake which is a few diameters long. The quantity of interest is the tip of the cylinder transverse displacements. A Matlab image processing script detects the cylinder tip. The frames sequence is first converted to 8bit black and white images and binarized with a threshold, to separate the cylinder from the background. A quadratic regression curve is then fitted on the cylinder pixels to follow its center line. The tip stands on the end of this regression line. We estimate the detection error of the tip 1 pixel $= 0.1$ mm. As the displacements are normalized by the cylinder diameter D, the error is 2%. Each root mean square value of a 20-

<table>
<tr><th>Parameter</th><th>Example 1</th><th>Example 2</th><th>Example 3</th><th>Example 4</th><th>Example 5</th></tr>
<tr><td colspan="6">Dimensional</td></tr>
<tr><td>ℓ (mm)</td><td>200</td><td>1000</td><td>37800</td><td colspan="2">150</td></tr>
<tr><td>D (mm)</td><td>10</td><td>1</td><td>27</td><td colspan="2">5</td></tr>
<tr><td>E (GPa)</td><td>0.5</td><td>50</td><td>36.2</td><td colspan="2">0.014</td></tr>
<tr><td>Θ (kN)</td><td>0</td><td>0</td><td>5</td><td colspan="2">0</td></tr>
<tr><td>ρ (kg/m^3)</td><td>1000</td><td>1000</td><td>1600</td><td colspan="2">792</td></tr>
<tr><td>ρ_{f} (kg/m^3)</td><td colspan="5">1000</td></tr>
<tr><td>U (m/s)</td><td>0.05</td><td>N/A</td><td>0.4</td><td colspan="2">N/A</td></tr>
<tr><td colspan="6">Dimensionless</td></tr>
<tr><td>$\mathcal{M}$</td><td>1</td><td>1</td><td>1.6</td><td colspan="2">0.79</td></tr>
<tr><td>Γ</td><td>20</td><td>1000</td><td>1400</td><td colspan="2">30</td></tr>
<tr><td>S_t</td><td colspan="5">0.2</td></tr>
<tr><td>C_D^0</td><td>1.2</td><td>2</td><td>1.2</td><td colspan="2">N/A</td></tr>
<tr><td>C_{Di}^0</td><td>0.2</td><td>N/A</td><td colspan="3">0.2</td></tr>
<tr><td>C_L^0</td><td colspan="5">0.3</td></tr>
<tr><td>A_p</td><td>96</td><td>N/A</td><td colspan="3">96</td></tr>
<tr><td>A_q</td><td colspan="5">12</td></tr>
<tr><td>ϵ_p</td><td>N/A</td><td>N/A</td><td colspan="3">0.02</td></tr>
<tr><td>ϵ_q</td><td>0.04</td><td>0.3</td><td>0.04</td><td colspan="2">0.04</td></tr>
</table>

Table 1: Dimensional and dimensionless parameters values for each example.

second recording counting more than 2000 values, the standard error becomes negligible compared to experiments repeatability.

3. Numerical Results

This section presents comparisons to validate the implementation of the model. For all the examples, the fluid considered is water. Gravitational and buoyancy forces are neglected. To ensure deterministic results, we initialize the wake variables p and q with a uniform value of 0.001. The stopping criteria have default values $\mathrm{tol}_{\,r} = 10^{-5}, \mathrm{tol}_{\,u} = 10^{-8}$.

In the subcritical range $300 < \mathrm{Re} < 1.5 \times 10^5$, the values of C_D^0, C_{Di}^0, C_L^0 and S_t for a fixed cylinder are commonly assumed constant [22, 25] with values given in Tab. 1. For all the examples, the fluid considered is water with density $\rho_{\mathrm{f}} = 10^3$ kg/m^3 and kinematic viscosity $\nu_{\mathrm{f}} = 10^{-6}$ mm^2/s. While Facchinetti et al. studied cross-flow VIV on a rigid cylinder and recommended $A_q = 12, \epsilon_q = 0.3$ from experiments, so that $A_q/\epsilon_q \approx 40$, calibrations from Ref.[62] showed that this ratio for coupled in-line/cross-flow VIV strongly depends on the structural damping and the mass ratio and can reach up to 2727. In this work, unless otherwise mentioned, empirical parameters of the wake-oscillator are set to $A_p = 96, A_q = 12, \epsilon_p = 0.02, \epsilon_q = 0.04$. This set of parameters is widely used for in-line/cross-flow WOM and have been validated for slender pipes [68, 40]. The frequencies are normalized by the

Mode number i	1	2	3
λ_i	1.87510	4.69409	7.85476

Table 2: Modal parameters for the first three modes of a flexible cantilever beam with constant cross section

first natural frequency f_1. The i^{th} mode natural frequency of a clamped-free cylinder in water is given by:

$$f_i = \frac{\lambda_i^2}{2\pi\ell^2}\sqrt{\frac{EI}{m_s + m_{\mathrm{a}}}}, \tag{26}$$

where λ_i is the modal parameter for the ith mode of vibration [9]. It's value for the three first modes are provided in Tab. 2. The codes are made publicly available on GitHub on this link

1. Example 1 - Verification of in-line and cross-flow VIV in small displacements

This example verifies the implementation of the in-line and cross-flow VIV on a single linear beam element with a semi-analytical solution.

The problem consists in a cantilever beam submitted to a transverse flow with a uniform and steady velocity $U\mathbf{e}_{\mathrm{x}}$ as illustrated in Fig. 3. The material has a Young modulus of E and a density ρ. The structure has a linear elastic behavior for the internal forces and a lumped mass formulation for the inertial terms. Additionally, we consider small displacements and no structural damping.

We only consider the transverse displacement in the yz-plane. The fluid has constant velocity U and exerts oscillating drag and lift forces. The parameter values are presented in Tab. 1.

Consider the distributed nonlinear drag and lift loads:

$$\mathbf{b}_d\left(p, \dot{u}_y, \dot{u}_y\right) = b_d\left(p, \dot{u}_y, \dot{u}_y\right)\mathbf{e}_{\mathrm{x}} = \frac{1}{2}\left(C_0^D + \frac{pC_i^D}{2}\right)\rho_{\mathrm{f}} D U_{\mathrm{rel}}^2, \tag{27}$$

$$\mathbf{b}_l\left(q, \dot{u}_x, \dot{u}_y\right) = b_l\left(q, \dot{u}_y, \dot{u}_y\right)\mathbf{e}_{\mathrm{y}} = \frac{1}{2}\frac{qC_0^L}{2}\rho_{\mathrm{f}} D U_{\mathrm{rel}}^2, \tag{28}$$

with the relative velocity $U_{\mathrm{rel}}^2 = \left(U^2 - \dot{u}_x/2\right)^2 + \left(\dot{u}_y/2\right)^2$. The nodal velocities are averaged to compute a relative velocity constant along the element. For this specific validation case, the change in load direction is neglected as small displacements are considered. The equivalent nodal forces and moments are given by the principle of virtual work. Considering a single linear Bernoulli beam element with length ℓ the equivalent nodal force and moment at the tip A are $\frac{1}{2}b_d\ell\mathbf{e}_{\mathrm{x}} + \frac{1}{2}b_l\ell\mathbf{e}_{\mathrm{y}}$ and $-\frac{1}{12}b_d\ell^2\mathbf{e}_{\mathrm{x}} + \frac{1}{12}b_l\ell^2\mathbf{e}_{\mathrm{y}}$ respectively [49]. The equation of motion of node A is:

$$\begin{bmatrix} m & 0 & 0 & 0 \\ 0 & 0 & 0 & 0 \\ 0 & 0 & m & 0 \\ 0 & 0 & 0 & 0 \end{bmatrix}\begin{bmatrix} \ddot{u}_y \\ \ddot{\theta}_x \\ \ddot{u}_x \\ \ddot{\theta}_y \end{bmatrix} + \frac{EI}{\ell^3}\begin{bmatrix} 12 & -6\ell & 0 & 0 \\ -6\ell & 4\ell^2 & 0 & 0 \\ 0 & 0 & 12 & 6\ell \\ 0 & 0 & 6\ell & 4\ell^2 \end{bmatrix}\begin{bmatrix} u_y \\ \theta_x \\ u_x \\ \theta_y \end{bmatrix} = \frac{1}{12}\begin{bmatrix} 6b_l\ell \\ -b_l\ell^2 \\ 6b_d\ell \\ b_d\ell^2 \end{bmatrix}, \tag{29}$$

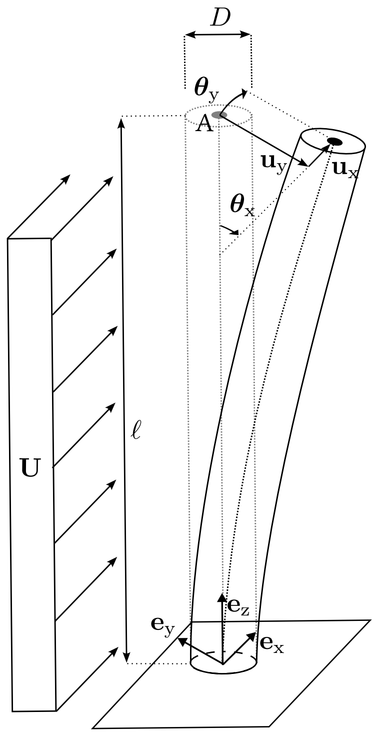

Figure 3: 3D view of the cantilever beam with small displacements.

where m corresponds to the lumped solid mass and fluid added mass at the free end:

$$m = \frac{1}{2}\left(m_{\mathrm{s}} + C_a \rho_{\mathrm{f}} \ell \pi \left(\frac{d}{2}\right)^2\right). \tag{30}$$

System (29) can be simplified to two equations:

$$m\ddot{u}_x + u_x \frac{12EI}{\ell^3} + \left(-\frac{b_d \ell}{8} - u_x \frac{9EI}{\ell^3}\right) = \frac{b_d \ell}{2}, \tag{31}$$

$$m\ddot{u}_y + u_y \frac{12EI}{\ell^3} + \left(\frac{b_l \ell}{8} - u_y \frac{9EI}{\ell^3}\right) = \frac{b_l \ell}{2}. \tag{32}$$

We set the equivalent stiffness $k_u = 3EI/\ell^3$. The reference system is:

$$\begin{cases} m\ddot{u}_x + k_u u_x = \dfrac{3b_d\ell}{8}, \\ m\ddot{u}_y + k_u u_y = \dfrac{3b_l\ell}{8}, \\ \ddot{p} = -2\epsilon_p\Omega_f^2(p^2-1)\dot{p} - 4\Omega_f^2 p + \dfrac{A_p}{D}\dfrac{\ddot{u}_x}{2}, \\ \ddot{q} = -\epsilon_q\Omega_f(q^2-1)\dot{q} - \Omega_f^2 q + \dfrac{A_q}{D}\dfrac{\ddot{u}_y}{2}. \end{cases} \tag{33}$$

This nonlinear reference solution is used to validate the amplitude displacements of the coupled variables (u_x, u_y, p, q). The Matlab function `ode45` using a 4^{th} order Rung-Kutta algorithm solves this nonlinear system.

System (33) is solved numerically over 2000 time steps. The relative error between the two solutions is defined by

$$\epsilon_{\mathbf{x}} = \frac{\|\mathbf{x}_{model} - \mathbf{x}_{ref}\|_2}{\|\mathbf{x}_{ref}\|_2}, \tag{34}$$

where $\mathbf{x}$ is a vector with the magnitude values for all the time steps. Using this metric, the errors for this simulation are displayed in Tab. 3. Fig. 4 compares temporal evolution of u_x, u_y, p, q from the model with the reference solution

Error	$\epsilon_{\mathbf{u}_x}$	$\epsilon_{\mathbf{u}_y}$	$\epsilon_{\mathbf{p}}$	$\epsilon_{\mathbf{q}}$
Value	0.29%	0.23%	0.15%	0.000087%

Table 3: Relative errors of u_x, u_y, p, q.

over one period T of the motion. The model follows closely the reference solution. The doubled vortex shedding pulsation in the in-line Van der Pol oscillator Eq. (16) causes a doubling of frequency of the oscillator p. The present model is in agreement with the reference solution and the relative errors of the four investigated quantities are below 0.3%.

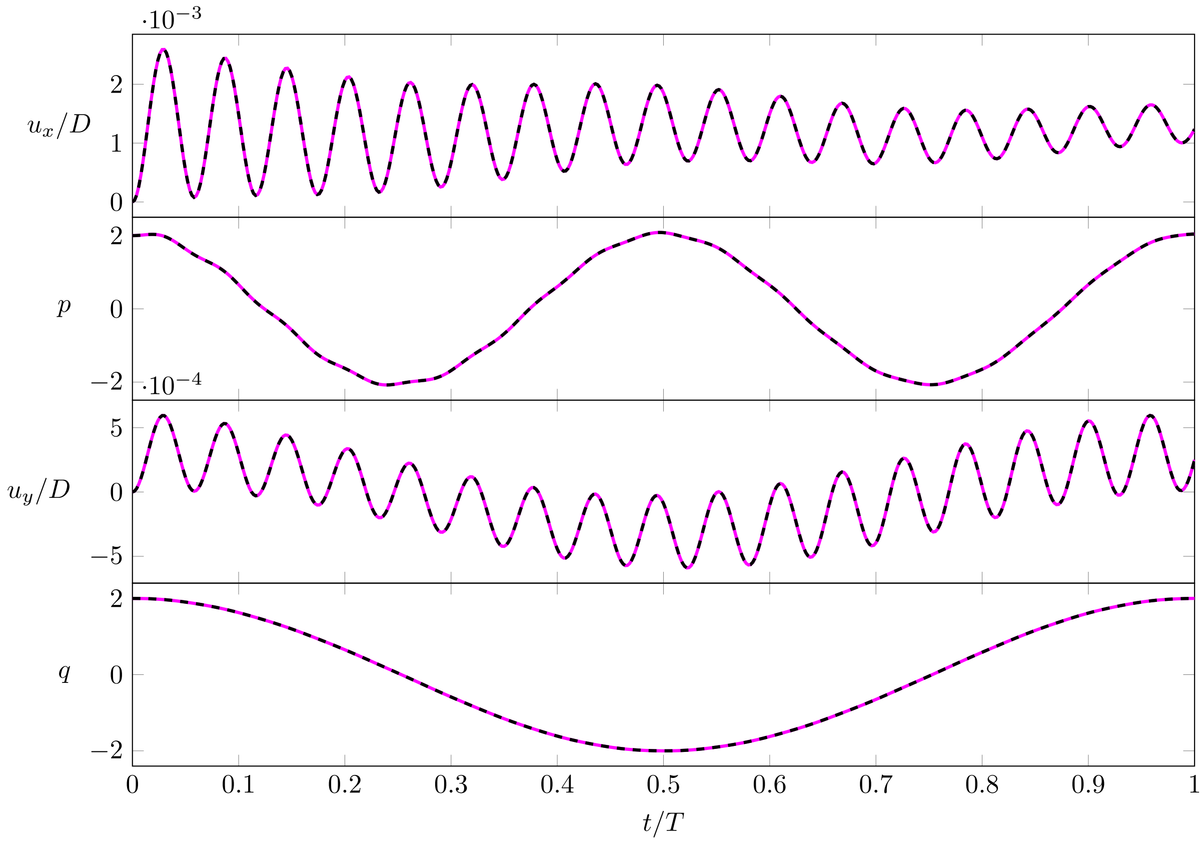

Figure 4: Verification of the in-line and cross-flow displacements u_x, u_y and wake variables p, q of a cantilever beam in a uniform flow with small displacements. Present model (- - -), Reference solution (——).

2. Example 2 - Validation of cross-flow VIV with large displacements

This example validates the cross-flow VIV model in large displacements with Leclercq and de Langre wake-oscillator.

A cantilever beam of length ℓ, density ρ and uniform circular cross section with diameter D is clamped at one end. It bends under a transverse uniform and steady flow of velocity $\mathbf{U} = U\mathbf{e}_{\mathrm{x}}$ and density ρ_{f} (see Tab. 1 for exact values). The beam bends in the xz-plane with large deformation and undergoes cross-flow vibrations along $\mathbf{e}_{\mathrm{y}}$ as displayed on Fig. 3. In this specific validation example, in-line VIV forces are neglected: the drag coefficient takes the constant value $C_D = 2$. The wake-oscillator parameters for cross-flow VIV are $A_q = 12, \epsilon_q = 0.3$ as recommended in Ref.[22] and used by Leclercq and de Langre.

The beam is discretized in 100 elements and the time using 10^6 time steps. The static solution is first computed with increasing reduced velocity. The dynamic problem is then solved using the steady solution as the initial configuration. The analysis considers only the second half of the simulation. This cuts off the transient and allows the vibrational dynamics to build up. The amplitudes are normalized by D and the frequencies by the first structural frequency f_1 obtained by Eq. (26). The root mean square amplitudes and frequencies of the transverse displacement of the cylinder tip are compared in Figs (5,6), respectively. Note that the definition of U_R used in Ref.[38] incorporates the Strouhal number $S_t = 0.2$, resulting in a stretching of the x-axis by a factor of 5.

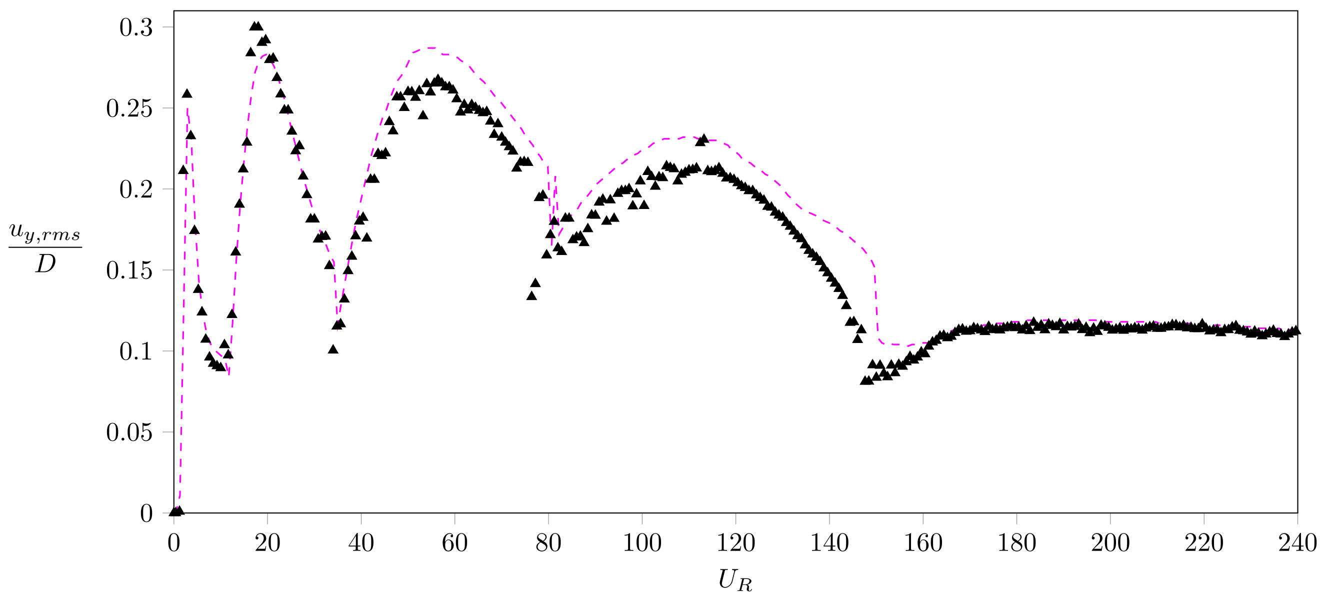

Figure 5: Cross-flow RMS amplitude of the tip of the cylinder: present model (▲); Ref.[38] data (– – –).

For small deflections ($U_R < 150$), the cylinder is excited with single-mode lock-in: the peaks of amplitude at $U_R = 2.8$, $U_R = 18$, $U_R = 56$ and $U_R = 110$ in Fig. 5 correspond to the lock-in between the wake frequency and the first, second, third and fourth modes respectively. At those values, only one frequency is excited (Fig. 6). When

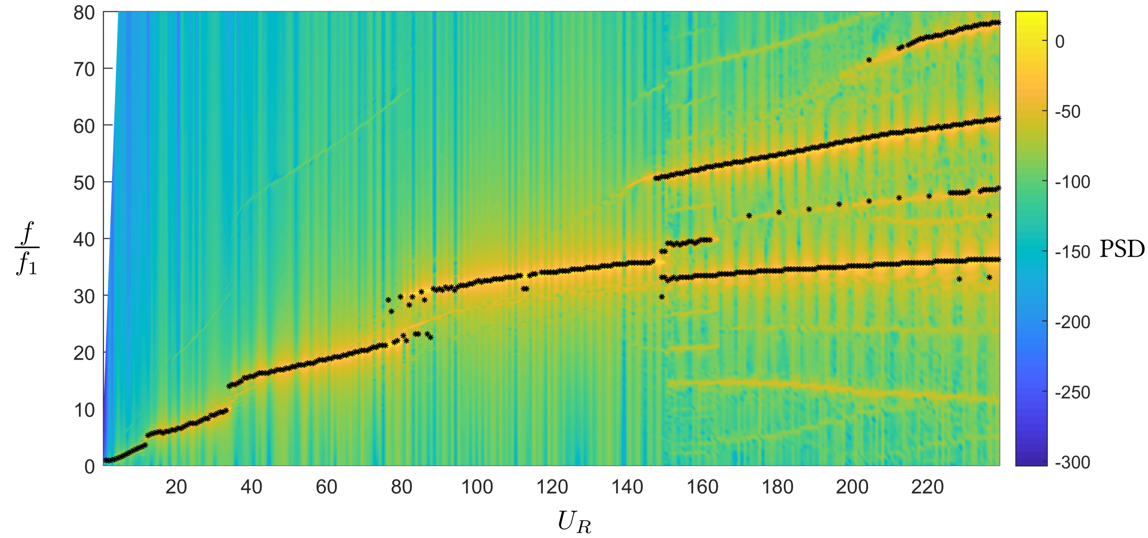

Figure 6: Cross-flow displacements of the cylinder tip: dominating frequencies from the present model ($*$) is plotted over the power spectral density (PSD) spectrogram from the Matlab code used in Ref.[38].

the deflection is large enough ($U_R > 150$), the transverse amplitudes reach a lower constant value of 0.1 (Fig. 5) and several frequencies are excited at the same time (Fig. 6). The variations in the normal flow profile along the span of the structure induces a lower and multi-frequency response compared with uniform flow, as described in Ref.[38].

The present model is capable of reproducing the same amplitudes and frequencies as in Ref.[38] up to reduced velocities as large as $U_R = 240$, validating the cross-flow VIV in large displacements and large rotations.

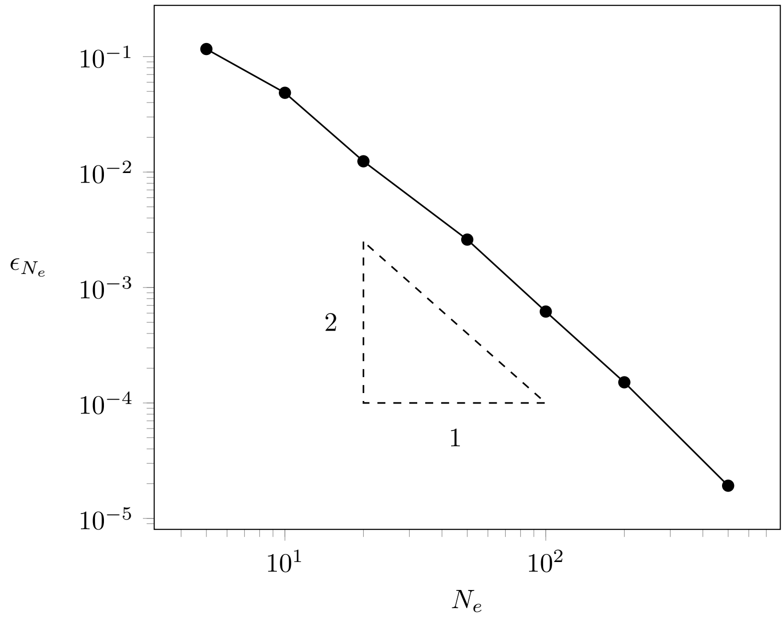

Figure 7: Mesh analysis with a reference solution of 1000 elements (—●—).

3. *Example 3 - Validation of in-line VIV*

This example aims to validate the implementation of the in-line and cross-flow wake-oscillator model against experimental results form Ref.[65] and DNS results from Ref.[31].

We study a cantilever hollow pipe of length $\ell = 37.8$ m, external diameter $D = 27$ mm and internal diameter $D_{\text{int}} = 21$ mm. It has pinned boundary conditions at both ends. Riser tension is constant, set to $\Theta = 5$ kN (even if experimental measurements show oscillations between 4 kN and 6 kN). The uniform and steady current has a velocity U and flows transverse to the pipe. The other parameters are summarized in Tab. 1.

A mesh analysis is performed on this example in order to estimate the number of elements needed to accurately solve both in-line and cross-flow VIV.

We then compare the numerical displacements $\mathbf{d}_{N_e}(x,t)$ with a reference solution $\mathbf{d}_{ref}(x,t)$ over $N_t = 1000$ time steps, equivalent to 20 periods of motion. The comparison is performed for different numbers of elements, $N_e = 1000$ being the reference value. The relative error between the displacement histories is given by:

$$\epsilon_{N_e} = \frac{\int_0^\ell \int_0^{t_f} \|\mathbf{u}_{N_e}(x,t) - \mathbf{u}_{ref}(x,t)\|_1 dtdx}{\int_0^\ell \int_0^{t_f} \|\mathbf{u}_{ref}(x,t)\|_1 dtdx}. \tag{35}$$

Figure 7 displays the evolution of the relative error with N_e. The error is inversely proportional to the square of the number of elements: $\epsilon_{N_e} \sim 1/N_e^2$. In this example, $N_e = 100$ is enough to have an error $\epsilon_{N_e} < 10^{-3}$.

Numerical results are presented with the reference solution $N_e = 1000$ in Figure 8. The first half of the simulation is ignored in the analysis to cut out the transient. RMS values of both cross-flow and in-line displacements along the

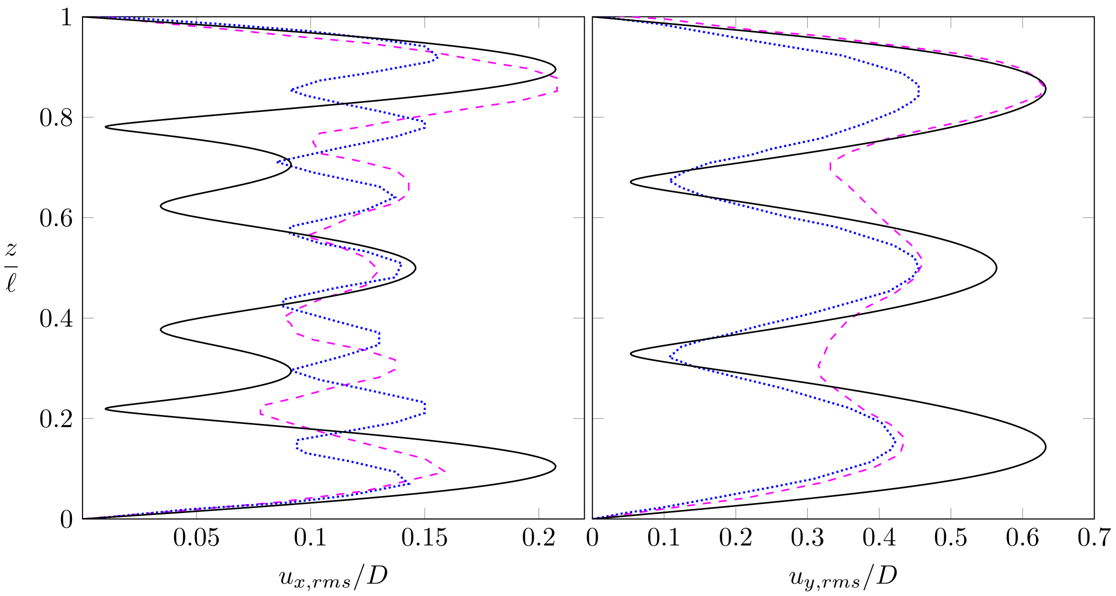

Figure 8: In-line and cross-flow RMS displacements along the pipe. Present model (——), experimental data from Ref.[65] (- - -), DNS data from [31] (⋯⋯).

span are compared to experimental results from Ref.[65] as well as DNS simulation from Ref.[31]. The fifth mode emerges as the dominant in-line mode in both the model and experimental data, while the third mode remains the dominant cross-flow mode in all the presented data. The symmetry of the problem about the pipe midpoint leads to a symmetric response of the pipe. This differs from the richer experimental response, underlying the complexity of the VIV process.

The maximum RMS displacement is predicted with a relative error of 0.4% for in-line and 0.2% for cross-flow compared with the experimental data. This is often a quantity of interest when assessing structural fatigue from VIV [24], well estimated by this simple numerical model. We obtain general agreement with the experimental data from Ref.[65].

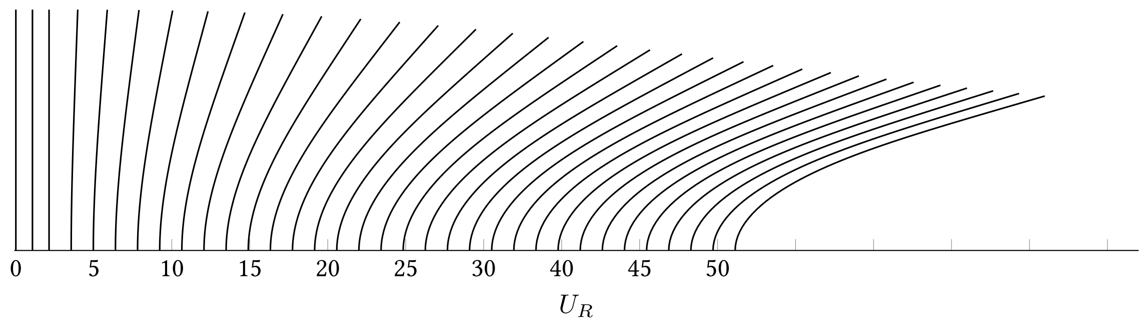

Figure 9: Cylinder center line static deflection in xz-plane with increasing U_R.

4. *Example 4 - Experimental validation*

This example compares the model with lab experimental data obtained following the experimental methodology described in Section 2.

A cylinder is submitted to a transverse flow with a constant and uniform velocity U with clamped and free ends. The simulation and experimental parameters are displayed in Tab. 1. The cylinder has a length ℓ, diameter D and bending stiffness EI. Unlike previous examples, the mass ratio is lower than 1: $\mathcal{M} = 0.79$. To account for the Reynolds number effect on the drag, the constant drag coefficient C_D^0 follows the empirical model for a circular cross section from Ref.[12]:

$$C_D^0(R_\mathrm{e}) = 11R_\mathrm{e}^{-0.75} + 0.9\left(1 - e^{-1000/R_\mathrm{e}}\right) + 1.2\left(1 - e^{-(R_\mathrm{e}/4500)^{0.7}}\right). \tag{36}$$

Fig. 9 plots the cylinder center line in the xz-plane for increasing U_R, providing a visual representation of the deformations.

The experimental data are compared with the numerical results. Fig. 10 displays the transverse RMS amplitudes of the tip $u_{y,rms}/D$ over the range of interest $U_R = [0, 50]$. During the intermediate flow regimes between the two lock-ins, the cylinder experiences very low oscillations, with the experimental RMS amplitude dropping below 0.1 for $U_R \in [8.5, 14.3]$, and after the second lock-in for $U_R > 39$ (Fig. 10). In Eq. (36), the drag coefficient decreases with the reduced velocity, which might explain the higher amplitudes observed during the second lock-in.

Fig. 11 presents the spanwise localization of the RMS transverse amplitudes obtained from simulations for varying reduced velocities. The transverse beam shapes are plotted for two different flow velocities: $U_R = 4.5$ and $U_R = 18$. In the first lock-in, the vibration is dominated by the first mode, while in the second lock-in, mode 2 becomes predominant. The ranges of U_R where the first and second lock-in occur in the simulation are coloured with pink and purple rectangles, respectively. First and second lock-ins occur on the range $U_R = [1.7, 7.8]$ and $U_R = [11, 50]$ respectively, with a gap in between the two lock-ins where the cylinder almost doesn't vibrate. Fig. 12 displays the frequencies PSD of the tip transverse displacements at different reduced velocities, as obtained from both simulation and experimental data. Fig. 12 also displays the vortex shedding frequency $f_w = S_t U/D$ and

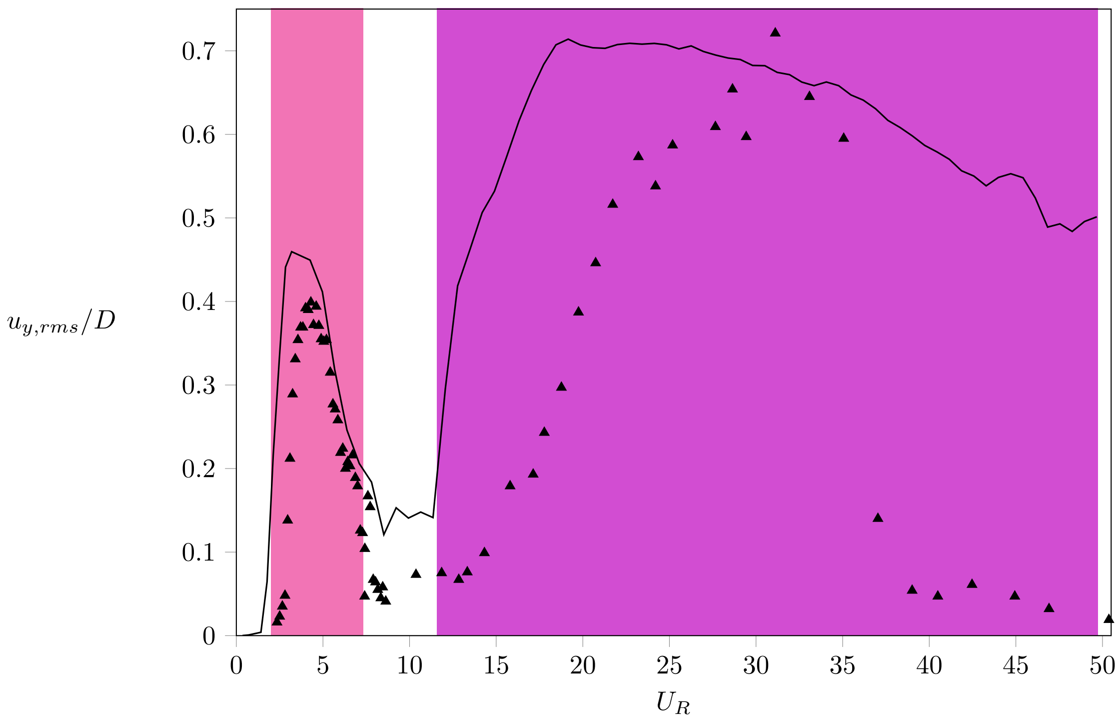

Figure 10: Cross-flow RMS displacements of the cylinder tip: present model (——), experimental data (▲). Pink and purple regions represent the mode 1 and 2 lock-in ranges, respectively, where $u_{y,rms} < 0.2D$.

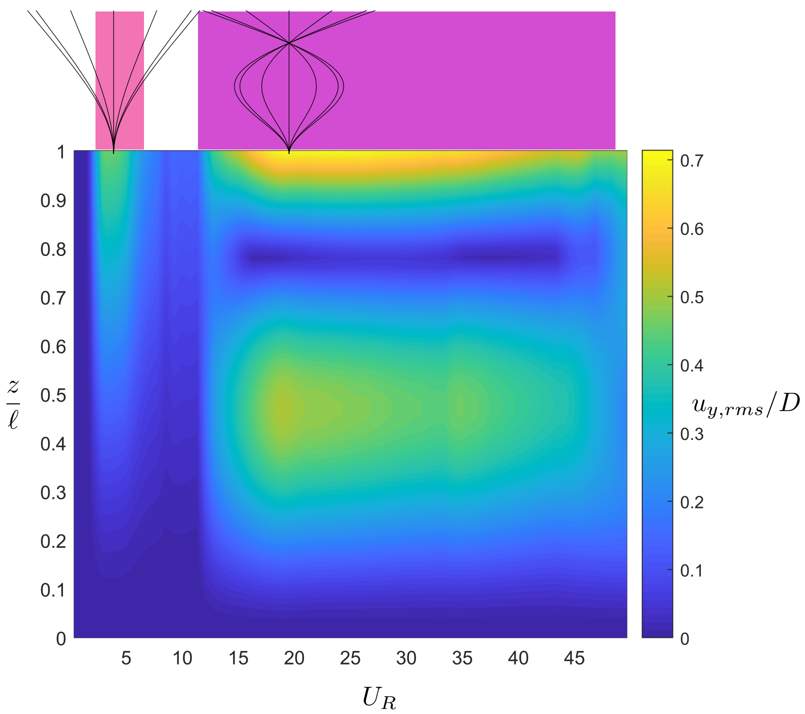

Figure 11: Spanwise localization of the RMS transverse displacement for varying U_R. Beam shapes transverse displacements (—) appear for $U_R = 4.5$ and $U_R = 18$. Pink and purple regions represent the mode 1 and 2 lock-in ranges, respectively, where $u_{y,rms} < 0.2D$.

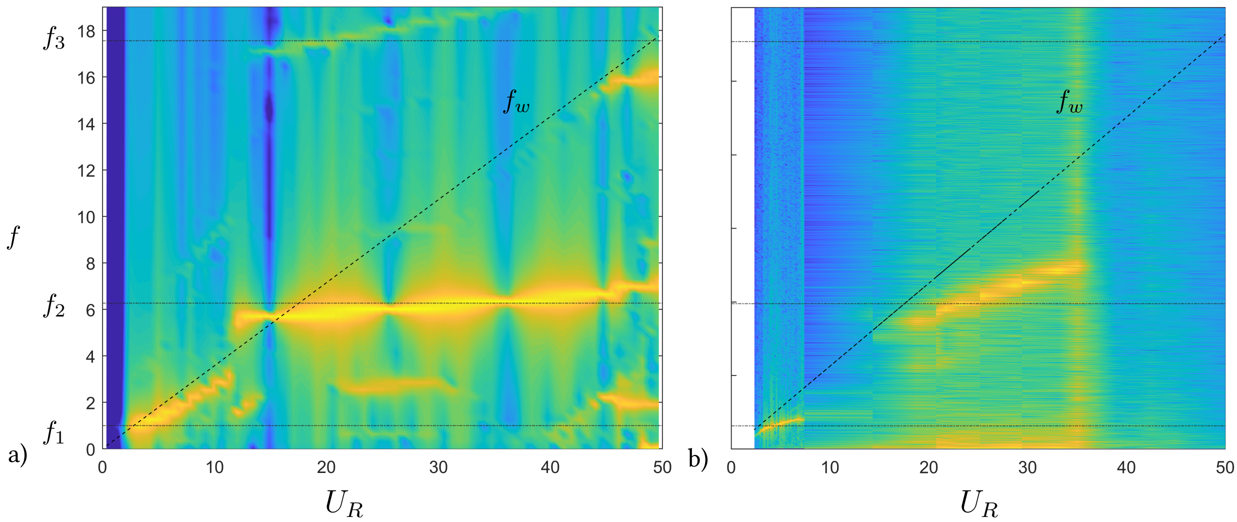

Figure 12: Spectrograms of the cross-flow displacements of the cylinder tip from the present model (a) and experimental data (b). All frequencies are normalized by f_1.

the three first natural frequencies of the cylinder f_1, f_2, f_3 on horizontal dotted lines, computed with Eq. (26). All the frequencies are normalized by $f_1 = 2.7$ Hz.

The main excited frequency in the simulation follows at first the vortex shedding frequency (Fig. 12), and a strong lock-in on f_2 is observed for $U_R > 12$. The first two lock-in ranges in Fig. 12(a) are dominated with a single frequency, while a multi-frequency response appears for $U_R > 45$. This multi-frequency response was observed by Leclercq and de Langre for $U_R > 150$ in Fig. 6. In a large deflection case, as the elements are closer to the tip they perceive a decreasing normal flow velocity. Thus, when moving towards the tip, the structure is excited by the wake at a decreasing frequency. This spreading of the wake excitation spectrum during large deformations is thus attributed to the variations in the spanwise profile of the normal free-stream component [38]. This feature is also captured in our model.

The proposed model effectively captures the overall physics of VIV measured experimentally. Figs 10, 12 demonstrate that the model accurately represents the tip amplitudes, frequencies and the right mode number for the first and second lock-in ranges. The observed decrease in vibration between them is also present. The relative errors on the tip transverse maximum RMS amplitude in Fig. 10 for the first and second lock-in ranges are 19.6% and 0.9%, respectively. However the second one is predicted on a wider range of U_R than the experimental data. Note that the WOM empirical parameters could be optimized for this specific study to improve the prediction, but it is beyond the scope of this work.

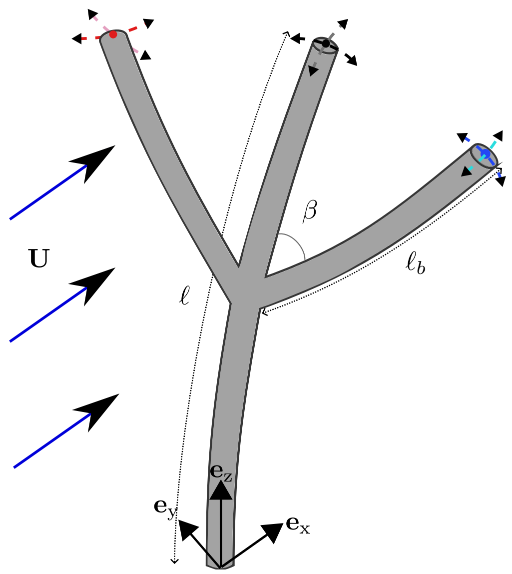

Figure 13: Coral geometry with two branches. Arrows at the tips indicate for each branch the in-line direction (lighter color) and cross-flow direction (darker color)

5. *Example 5 - Branching structure*

This example presents an application of the model to structures with branching features and constitutes a novel contribution as it is the first time the WOM has been applied to such structures. The planar branched geometry is inspired by the gorgonian soft coral *Antillogorgia bipinnata*, which grows perpendicular to the ambient flow [54].

The materials and method are the same as in Example 4. The only difference is the structure geometry: one pair of symmetric branches with an angle of $\beta = 60^\circ$ and length $\ell_b = 0.08$ m is added to the straight cylinder. Fig. 13 displays the problem geometry. The planar structure is placed perpendicular to the flow in the initial configuration and the flow velocity is increased by steps.

The in-line displacement at all nodes is u_x. We define the transverse displacements of the nodes located at the tips of the trunk, the right and left branches respectively as:

$$u_t^{\text{trunk}} = u_y, \tag{37}$$

$$u_t^{\text{b1}} = \cos(\beta) u_y - \sin(\beta) u_z, \tag{38}$$

$$u_t^{\text{b2}} = \cos(\beta) u_y + \sin(\beta) u_z. \tag{39}$$

We keep the definition of the reduced velocity: $U_R = U\ell^2 D^{-1}(m + m_a)^{1/2}(EI)^{-1/2}$ using the initial height of the structure ℓ.

Fig. 14 displays the coral displacements with two point of views over half a period of the motion at chosen reduced velocities: $U_{R,1} = 2.0$, $U_{R,2} = 6.5$, $U_{R,3} = 13$, $U_{R,4} = 19.6$, $U_{R,5} = 29.3$, $U_{R,6} = 39.9$. The in-line and cross-flow displacements RMS amplitude against U_R are displayed in Fig. 15. The two branches tip RMS amplitudes are similar,

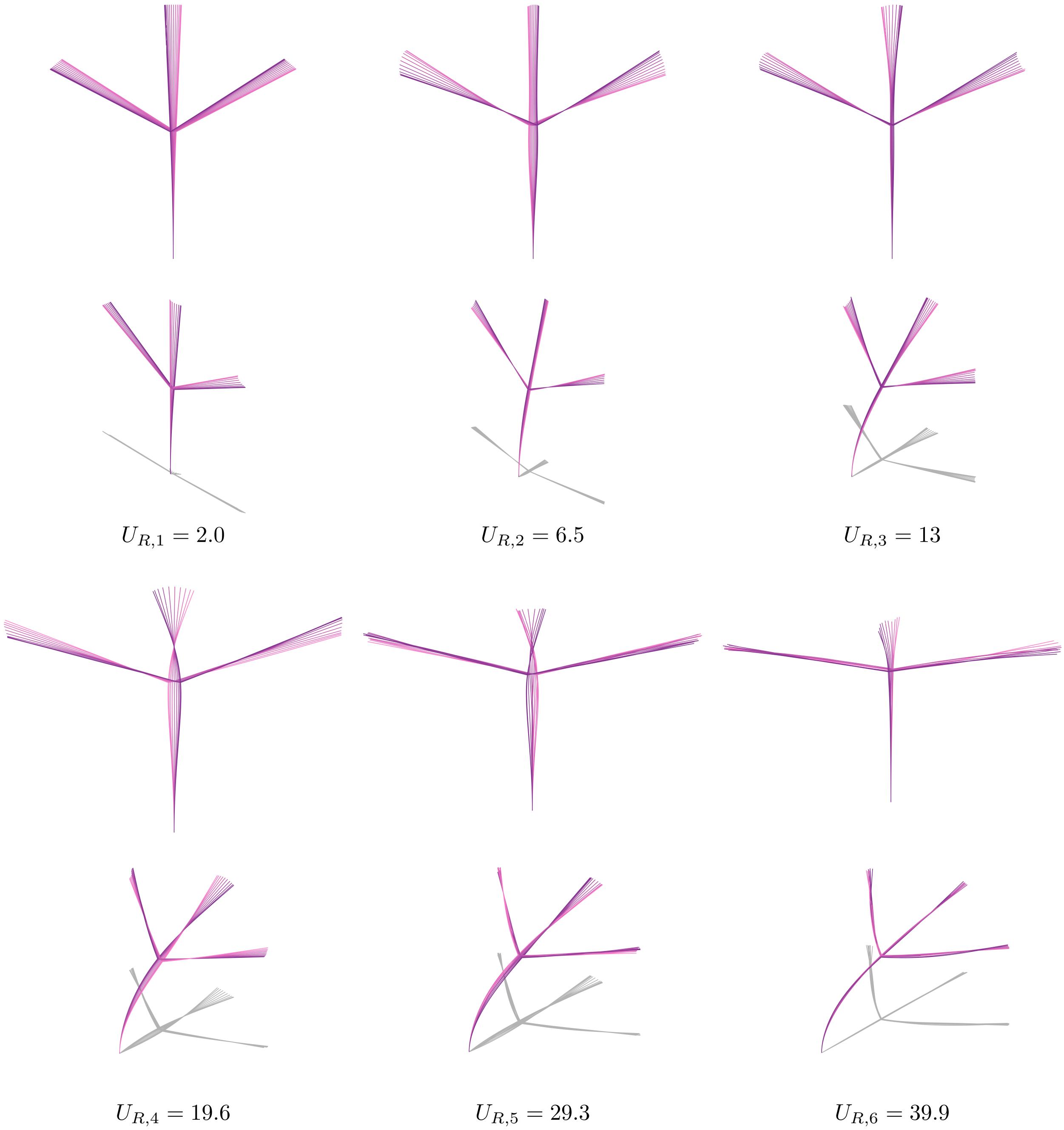

Figure 14: Shape of the structure motion at the end of the simulation for different reduced velocities. The 3D point of view is pointing towards the vector [-1 -1 1]

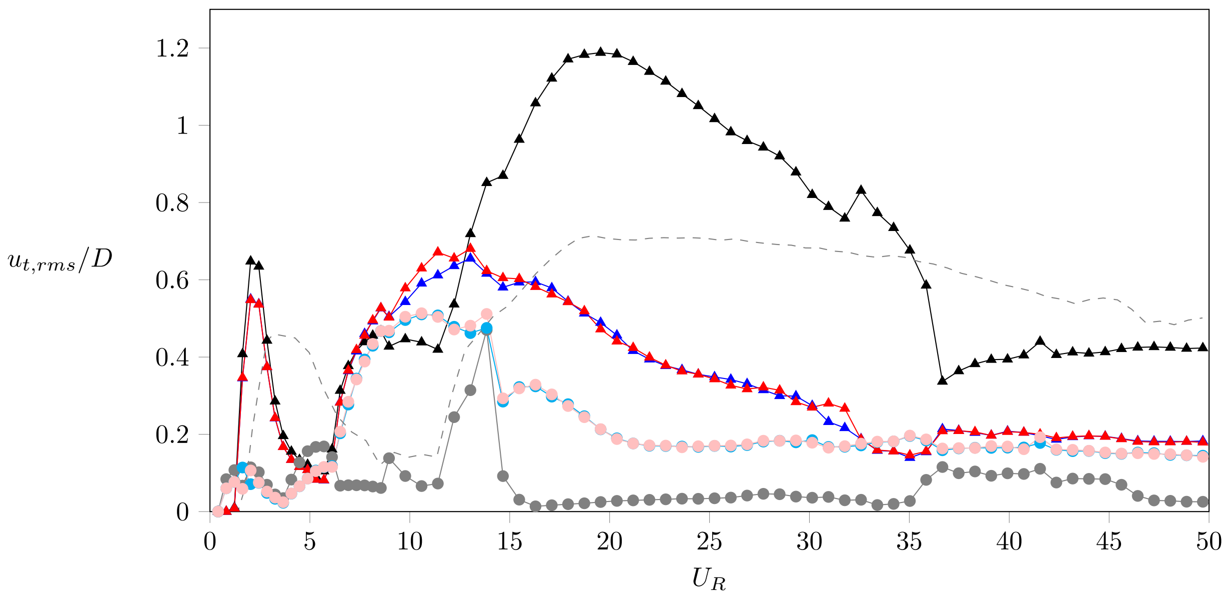

Figure 15: In-line RMS displacements of the cylinder tips from simulations: trunk tip (—●—), left branch tip (—●—), right branch tip (—●—). Cross-flow RMS displacements of the cylinder tips from simulations: trunk tip (—▲—), left branch tip (—▲—), right branch tip (—▲—), previous example (– – –).

which is relevant with the problem symmetry. The two main peaks of the trunk tip transverse amplitude occur at $U_R \sim 2$ and $U_R \sim 20$, just as in the previous example for the cylinder. However, the two peaks are much higher: up to $0.6D$ and $1.2D$. The magnitude of the in-line displacements is comparable to that of the transverse displacements within the range $U_R \in [6 - 9]$. In order to explain these observations, we study the excited frequencies.

The spectrograms presented in Fig. 16(a,b) depict the PSD of the in-line and cross-flow displacements at the right branch tip, respectively, as a function of U_R. Additionally, in-line and cross-flow vortex shedding frequencies $2f_w$ and f_w, respectively, are presented. The spectrogram from the left branch (not displayed here) is visually indistinguishable from the right branch.

The in-line spectrogram in Fig. 16(a) presents several frequencies aligning with the $2f_w$ line for $U_R \in [5 - 10]$, exhibiting distinct jumps indicative of lock-in regions succession. The stronger lock-in regions on the doubled vortex shedding frequency is consistent with the doubled frequency model in the in-line oscillator Eq. 20. The corals shapes at these frequencies (Fig. 14, $U_{R,1} = 2.0$, $U_{R,2} = 6.5$) indeed suggest that vibration mode transitions occur in this range. At low reduced velocities, the coral exhibits transverse vibrations without independent motion of the branches (Fig. 14, $U_{R,1} = 2.0$). This first mode of vibration explains the first amplitude peak of transverse vibrations, while the in-line amplitudes remain small (Fig. 15). This is consistent with the high PSD region in the cross-flow spectrogram, absent in the in-line spectrogram (Fig. 16). For low reduced velocities, lock-in occurs mainly on the transverse displacements. The presence of the two branches contributes to increased lift in this vibration mode. As a result, the transverse RMS amplitudes increase from $0.47D$ for the cylinder in the previous example to $0.65D$ here. The second peak of amplitude occurs at $U_R = 20$ where the trunk vibrates with a mode 2 (Fig. 14). At $U_R = 20$,

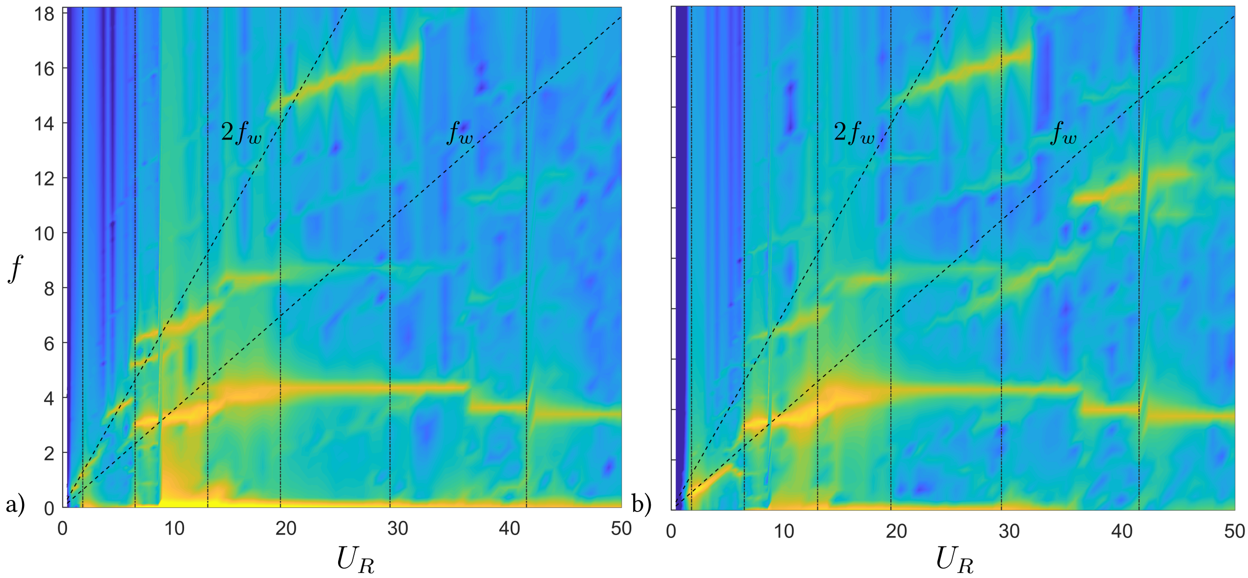

Figure 16: Spectrogram of the in-line (a) and cross-flow (b) displacements at the tip of the right branch. Vertical lines ($-\cdot$) are plotted for $U_{R,1-6} = 2.0, 6.5, 13, 19.5, 29.3, 39.9$. Frequencies are normalized by the first bending frequency of a cylinder in water f_1.

RMS transverse amplitudes reach up to $1.2D$, compared to $0.7D$ for the straight cylinder.

In contrast to the straight cylinder case where the natural frequencies of the structure are excited one at a time for $U_R < 45$, a notable difference is observed in the case of branched structures. Here, a multi-frequency response emerges for $U_{R,6} < 6.5$, indicating simultaneous excitation of multiple natural frequencies. By adding branches to the structure, the modal response of the structure is modified and several frequencies can be excited at the same reduced velocity, causing a multi-frequency response (Fig. 16). Increased vibrations amplitudes are observed, emphasizing the crucial role of VIV in branched structures.

4. Discussion and conclusion

This study aims to extend the capabilities of the WOM by developing a new formulation that accounts for coupled in-line and cross-flow VIV in branching structures. We provide a simple yet accurate tool for simulating 3D fluid-structure interaction problems. The proposed finite element corotational formulation allows to simulate arbitrarily complex beam structures, including tree-like geometries. This constitutes the main novelty of this paper since previous applications of the WOM are restricted to straight geometries such as pipes or cylinders. It also integrates the WOM and added mass effects into the corotational framework. The numerical resolution of the proposed formulation is implemented and made publicly available in the open-source FEM library ONSAS.

The present model is verified and validated through a comprehensive analysis involving four examples of a clamped-free flexible cantilever cylinder in a uniform flow.

In Example 1, the in-line and cross-flow VIV formulation is verified against a semi-analytical solution in small displacements. In Example 2, the cross-flow VIV model is validated in large displacements against existing wake-oscillator simulation results. In Example 3, the in-line and cross-flow VIV model is validated against experimental data from the literature. A mesh analysis is also conducted, revealing a second-order convergence. In Example 4, our own experimental data are compared to the model. The maximum RMS transverse amplitudes are well predicted, yet the velocity range of the second lock-in is overestimated. Eventually, two branches are added in Example 5 and the amplitudes and frequency of the trunk and branch tips are presented. This study represents the first application of the WOM on a structure with branches.

Our analysis reveals that compliant branched structures subjected to flow exhibit a multi-frequency response with high amplitude of vibrations. The branching leads to a richer and denser spectrum of natural frequencies. We could expect soft corals and other branched structures to exhibit a rich multi-frequency dynamics.

Future work can explore the effect of the wake variable interpolation order on element accuracy. It would be valuable to validate the formulation with a fully coupled FSI study of a branched structure. Carrying a modal analysis of the branched structure can enlighten the complex interaction between the structure and the wake.

Overall, this study highlights the potential of the wake-oscillator model combined with the corotational approach for predicting VIV in complex geometries, and opens new avenues for the numerical study of the vortex-induced dynamics of branched structures and tree-like organisms.

Acknowledgments

The authors gratefully acknowledge the funding from the *Génie par Simulation* program, as well as NSERC Discovery Grants No. RGPIN-2019-07072. The authors would like to thank Dr. Tristan Leclercq for providing his Matlab code used for generating his data in [38].

References

[1] Yasuhiro Akagi and Katsuhiro Kitajima. Computer animation of swaying trees based on physical simulation. *Computers & Graphics*, 30: 529–539, 2006.

[2] Klaus-Jürgen Bathe. *Finite element procedures.* Klaus-Jurgen Bathe, 2006.

[3] Jean-Marc Battini and Costin Pacoste. Co-rotational beam elements with warping effects in instability problems. *Computer Methods in Applied Mechanics and Engineering*, 191(17-18):1755–1789, 2002.

[4] Heather R Beem and Michael S Triantafyllou. Wake-induced 'slaloming'response explains exquisite sensitivity of seal whisker-like sensors. *Journal of Fluid Mechanics*, 783:306–322, 2015.

[5] Michael M. Bernitsas, Kamaldev Raghavan, Y. Ben-Simon, and E. M. Garcia. VIVACE (Vortex Induced Vibration Aquatic Clean Energy): A New Concept in Generation of Clean and Renewable Energy From Fluid Flow. *Journal of Offshore Mechanics and Arctic Engineering*, 130(4): 041101–041101, September 2008. ISSN 0892-7219. doi: 10.1115/1.2957913. URL `http://dx.doi.org/10.1115/1.2957913`.

[6] Richard Evelyn Donohue Bishop and A. Y. Hassan. The lift and drag forces on a circular cylinder oscillating in a flowing fluid. *Proc. R. Soc. Lond. A*, 277(1368):51–75, January 1964. ISSN 0080-4630, 2053-9169. doi: 10.1098/rspa.1964.0005. URL `http://rspa.royalsocietypublishing.org/content/277/1368/51`.

[7] Robert D Blevins. Flow-induced vibration. *New York*, 1977.

[8] Robert D. Blevins. *Flow-induced vibration.* Van Nostrand Reinhold, 1990. ISBN 978-0-442-20651-2. URL `https://books.google.ca/books?id=yJ9RAAAAMAAJ`.

[9] Robert D Blevins. *Formulas for dynamics, acoustics and vibration.* John Wiley & Sons, 2015.

[10] Mouad Boudina, Frédérick P., and Stéphane Étienne. Vortex-induced vibrations: a soft coral feeding strategy? *Journal of Fluid Mechanics*, 916:A50, 2021.

[11] J. R. Chaplin, P. W. Bearman, F. J. Huera Huarte, and R. J. Pattenden. Laboratory measurements of vortex-induced vibrations of a vertical tension riser in a stepped current. *Journal of Fluids and Structures*, 21(1):3–24, November 2005. ISSN 0889-9746. doi: 10.1016/j.jfluidstructs.2005.04.010. URL `http://www.sciencedirect.com/science/article/pii/S0889974605001465`.

[12] Nian-Sheng Cheng. Calculation of drag coefficient for arrays of emergent circular cylinders with pseudofluid model. *Journal of Hydraulic Engineering*, 139(6):602–611, 2013.

[13] Amir Chizfahm and Rajeev Jaiman. Data-driven stability analysis and near-wake jet control for the vortex-induced vibration of a sphere. *Physics of Fluids*, 33(4):044104, 2021.

[14] Haeseong Cho, DuHyun Gong, Namhun Lee, SangJoon Shin, and Seungsoo Lee. Combined co-rotational beam/shell elements for fluid–structure interaction analysis of insect-like flapping wing. *Nonlinear Dynamics*, 97:203–224, 2019.

[15] MA Crisfield, U Galvanetto, and G Jelenić. Dynamics of 3-d co-rotational beams. *Computational Mechanics*, 20(6):507–519, 1997.

[16] Emmanuel De Langre. Effects of wind on plants. *Annu. Rev. Fluid Mech.*, 40:141–168, 2008.

[17] Emmanuel De Langre. Methodological advances in predicting flow-induced dynamics of plants using mechanical-engineering theory. *Journal of Experimental Biology*, 215(6):914–921, 2012.

[18] Christelle Der Loughian, Loïc Tadrist, Jean-Marc Allain, Julien Diener, Bruno Moulia, and Emmanuel de Langre. Measuring local and global vibration modes in model plants. *Comptes Rendus Mécanique*, 342(1):1–7, January 2014. ISSN 16310721. doi: 10.1016/j.crme.2013.10.010. URL `https://linkinghub.elsevier.com/retrieve/pii/S1631072113001319`.

[19] Hesham A Elkaranshawy, Ahmed AH Elerian, and Walied I Hussien. A corotational formulation based on hamilton's principle for geometrically nonlinear thin and thick planar beams and frames. *Mathematical Problems in Engineering*, 2018, 2018.

[20] Constantinos Evangelinos and George Em Karniadakis. Dynamics and flow structures in the turbulent wake of rigid and flexible cylinders subject to vortex-induced vibrations. *Journal of fluid mechanics*, 400:91–124, 1999.

[21] Matteo Luca Facchinetti, Emmanuel de Langre, and Francis Biolley. Vortex-induced travelling waves along a cable. *European Journal of Mechanics - B/Fluids*, 23(1):199–208, January 2004. ISSN 0997-7546. doi: 10.1016/j.euromechflu.2003.04.004. URL `http://www.sciencedirect.com/science/article/pii/S099775460300102X`.

[22] M.L. Facchinetti, E. de Langre, and F. Biolley. Coupling of structure and wake oscillators in vortex-induced vibrations. *Journal of Fluids and Structures*, 19(2):123–140, feb 2004. ISSN 08899746. doi: 10.1016/j.jfluidstructs.2003.12.004. URL https://linkinghub.elsevier.com/retrieve/pii/S0889974603001853.

[23] Sigil Francis, V Umesh, and S Shivakumar. Design and analysis of vortex bladeless wind turbine. *Materials Today: Proceedings*, 47:5584–5588, 2021.

[24] Yun Gao, Shixiao Fu, Tie Ren, Youming Xiong, and Leijian Song. Viv response of a long flexible riser fitted with strakes in uniform and linearly sheared currents. *Applied Ocean Research*, 52:102–114, 2015.

[25] Yun Gao, Zhuangzhuang Zhang, Ganghui Pan, Geng Peng, Lei Liu, and Wei Wang. Three-dimensional vortex-induced vibrations of a circular cylinder predicted using a wake oscillator model. *Marine Structures*, 80:103078, 2021.

[26] Fei Ge, Xu Long, Lei Wang, and YouShi Hong. Flow-induced vibrations of long circular cylinders modeled by coupled nonlinear oscillators. *Science in China Series G: Physics, Mechanics and Astronomy*, 52(7):1086–1093, 2009.

[27] Frédérick P. Gosselin. Mechanics of a plant in fluid flow. *Journal of Experimental Botany*, 70(14):3533–3548, 2019.

[28] Ralf Habel, Alexander Kusternig, and Michael Wimmer. Physically guided animation of trees. In *Computer Graphics Forum*, volume 28, pages 523–532. Wiley Online Library, 2009.

[29] Wolf Hanke, Matthias Witte, Lars Miersch, Martin Brede, Johannes Oeffner, Mark Michael, Frederike Hanke, Alfred Leder, and Guido Dehnhardt. Harbor seal vibrissa morphology suppresses vortex-induced vibrations. *Journal of Experimental Biology*, 213(15):2665–2672, July 2010. doi: 10.1242/jeb.043216. URL http://jeb.biologists.org/content/213/15/2665.abstract.

[30] ROnald T. Hartlen and Iain G. Currie. Lift-Oscillator Model of Vortex-Induced Vibration. *Journal of the Engineering Mechanics Division*, 96 (5):577–591, 1970. URL https://cedb.asce.org/CEDBsearch/record.jsp?dockey=0016651. Publisher: ASCE.

[31] Samuel Holmes, Owen H Oakley Jr, and Yiannis Constantinides. Simulation of riser viv using fully three dimensional cfd simulations. *International Conference on Offshore Mechanics and Arctic Engineering*, 47497:563–570, 2006.

[32] Xiao-yi Hu, Wei-ming Tao, and Yi-mu Guo. Using fem to predict tree motion in a wind field. *Journal of Zhejiang University-Science A*, 9: 907–915, 2008.

[33] Anil Jain and Yahya Modarres-Sadeghi. Vortex-induced vibrations of a flexibly-mounted inclined cylinder. *Journal of Fluids and Structures*, 43:28–40, 2013.

[34] A Khalak and C. H. K Williamson. MOTIONS, FORCES AND MODE TRANSITIONS IN VORTEX-INDUCED VIBRATIONS AT LOW MASS-DAMPING. *Journal of Fluids and Structures*, 13(7):813–851, October 1999. ISSN 0889-9746. doi: 10.1006/jfls.1999.0236. URL http://www.sciencedirect.com/science/article/pii/S0889974699902360.

[35] Yun Zhi Law and Rajeev Kumar Jaiman. Wake stabilization mechanism of low-drag suppression devices for vortex-induced vibration. *Journal of Fluids and Structures*, 70:428–449, 2017.

[36] Thanh-Nam Le, Jean-Marc Battini, and Mohammed Hjiaj. Efficient formulation for dynamics of corotational 2d beams. *Computational Mechanics*, 48:153–161, 2011.

[37] Thanh-Nam Le, Jean-Marc Battini, and Mohammed Hjiaj. A consistent 3D corotational beam element for nonlinear dynamic analysis of flexible structures. *Computer Methods in Applied Mechanics and Engineering*, 269:538–565, feb 2014. ISSN 00457825. doi: 10.1016/j.cma.2013.11.007. URL http://linkinghub.elsevier.com/retrieve/pii/S0045782513003022.

[38] Tristan Leclercq and Emmanuel de Langre. Vortex-induced vibrations of cylinders bent by the flow. *Journal of Fluids and Structures*, 80:77–93, jul 2018. ISSN 08899746. doi: 10.1016/j.jfluidstructs.2018.03.008. URL https://linkinghub.elsevier.com/retrieve/pii/S0889974617307764.

[39] Jiarui Lei and Heidi Nepf. Wave damping by flexible vegetation: Connecting individual blade dynamics to the meadow scale. *Coastal Engineering*, 147:138–148, 2019.

[40] Xiaomin Li, Wenfei Wei, and Fengtao Bai. A full three-dimensional vortex-induced vibration prediction model for top-tensioned risers based on vector form intrinsic finite element method. *Ocean Engineering*, 218:108140, 2020.

[41] Orcina Ltd. *ORCAFLEX User manual*, 2007.

[42] Mitul Luhar and Heidi M Nepf. Flow-induced reconfiguration of buoyant and flexible aquatic vegetation. *Limnology and Oceanography*, 56 (6):2003–2017, 2011.

[43] Kathleen Lyons, Christin T Murphy, and Jennifer A Franck. Flow over seal whiskers: Importance of geometric features for force and frequency response. *Plos one*, 15(10):e0241142, 2020.

[44] Dror Malul, Roi Holzman, and Uri Shavit. Coral tentacle elasticity promotes an out-of-phase motion that improves mass transfer. *Proceedings of the Royal Society B: Biological Sciences*, 287(1929):20200180, June 2020. doi: 10.1098/rspb.2020.0180. URL https://royalsocietypublishing.org/doi/full/10.1098/rspb.2020.0180. Publisher: Royal Society.

[45] Dori McCombe and Josef D. Ackerman. Collector Motion Affects Particle Capture in Physical Models and in Wind Pollination. *The American Naturalist*, 192(1):81–93, July 2018. ISSN 0003-0147, 1537-5323. doi: 10.1086/697551. URL https://www.journals.uchicago.edu/doi/10.1086/697551.

[46] Florian Menter, Patrick Sharkey, Sergey Yakubov, and M Kuntz. Overview of fluid-structure coupling in ansys-cfx. In *International Conference on Offshore Mechanics and Arctic Engineering*, volume 47497, pages 579–585, 2006.

[47] Eduard Naudascher. *Flow-induced vibrations: an engineering guide.* Routledge, 2017.

[48] RHM Ogink and AV Metrikine. A wake oscillator with frequency dependent coupling for the modeling of vortex-induced vibration. *Journal of sound and vibration*, 329(26):5452–5473, 2010.

[49] Eugenio Oñate. *Structural analysis with the finite element method. Linear statics: volume 2: beams, plates and shells.* Springer Science & Business Media, 2013.

[50] Michael P Paidoussis. *Fluid-structure interactions: slender structures and axial flow*, volume 1. Academic press, 1998.

[51] Jorge M Pérez Zerpa, M. C. Vanzulli Pena, Alexandre Villié, Juan Bruno Bazzano García, Joaquin Viera Sosa, Marcelo Forets, and Jean-Marc Battini. Onsas.m: an open nonlinear structural analysis solver for gnu-octave/matlab, 2022. URL https://github.com/ONSAS/ONSAS.m.

[52] Yang Qu and Andrei V Metrikine. A single van der pol wake oscillator model for coupled cross-flow and in-line vortex-induced vibrations. *Ocean Engineering*, 196:106732, 2020.

[53] Ed Quigley, Yue Yu, Jingwei Huang, Winnie Lin, and Ronald Fedkiw. Real-time interactive tree animation. *IEEE transactions on visualization and computer graphics*, 24(5):1717–1727, 2017.

[54] Marta Ribes, Rafel Coma, and Josep-Maria Gili. Heterotrophic feeding by gorgonian corals with symbiotic zooxanthella. *Limnology and Oceanography*, 43(6):1170–1179, September 1998. ISSN 0024-3590. doi: 10.4319/lo.1998.43.6.1170. URL https://aslopubs.onlinelibrary.wiley.com/doi/abs/10.4319/lo.1998.43.6.1170. Publisher: John Wiley & Sons, Ltd.

[55] Mathieu Rodriguez, Emmanuel de Langre, and Bruno Moulia. A scaling law for the effects of architecture and allometry on tree vibration modes suggests a biological tuning to modal compartmentalization. *American Journal of Botany*, 95(12):1523–1537, December 2008. ISSN 1537-2197. doi: 10.3732/ajb.0800161. URL https://onlinelibrary.wiley.com/doi/abs/10.3732/ajb.0800161.

[56] Mathieu Rodriguez, Stéphane Ploquin, Bruno Moulia, and Emmanuel de Langre. The multimodal dynamics of a walnut tree: experiments and models. *Journal of Applied Mechanics*, 79(4):044505, 2012. URL https://manufacturingscience.asmedigitalcollection.asme.org/data/Journals/JAMCAV/26820/0445051.pdf.

[57] Turgut Sarpkaya. Vortex shedding and resistance in harmonic flow about smooth and rough circular cylinders at high reynolds numbers. Technical report, Naval Postgraduate School Monterey CA, 1976.

[58] H Sehat, M Abdolahpour, M Jamali, and M Ghisalberti. The impact of plant oscillation on dispersion in emergent aquatic canopies. *Water Resources Research*, page e2022WR032035, 2023.

[59] Mikio Shinya and Alain Fournier. Stochastic motion—motion under the influence of wind. In *Computer graphics forum*, volume 11, pages 119–128. Wiley Online Library, 1992.

[60] Richard A Skop and Sathish Balasubramanian. A new twist on an old model for vortex-excited vibrations. *Journal of Fluids and Structures*, 11(4):395–412, 1997.

[61] Thomas L. Spencer, Nina Mohebbi, Guangyuan Jin, Matthew L. Forister, Alexander Alexeev, and David L. Hu. Moth-inspired meth-

ods for particle capture on a cylinder. *Journal of Fluid Mechanics*, 884, 2019. ISSN 0022-1120, 1469-7645. doi: 10.1017/jfm.2019.927. URL https://www.cambridge.org/core/journals/journal-of-fluid-mechanics/article/mothinspired-methods-for-particle-capture-on-a-cylinder/FB655E925FD3745D1FBB2A9A6C2D3094. Publisher: Cambridge University Press.

[62] Narakorn Srinil and Hossein Zanganeh. Modelling of coupled cross-flow/in-line vortex-induced vibrations using double Duffing and van der Pol oscillators. *Ocean Engineering*, 53:83–97, oct 2012. ISSN 00298018. doi: 10.1016/j.oceaneng.2012.06.025. URL https://linkinghub.elsevier.com/retrieve/pii/S0029801812002296.

[63] Alexander Sukhodolov, Tatiana Sukhodolova, and Jochen Aberle. Modelling of flexible aquatic plants from silicone syntactic foams. *Journal of Hydraulic Research*, 60(1):173–181, 2022.

[64] Fang-Bao Tian, Hu Dai, Haoxiang Luo, James F Doyle, and Bernard Rousseau. Fluid–structure interaction involving large deformations: 3d simulations and applications to biological systems. *Journal of computational physics*, 258:451–469, 2014.

[65] AD Trim, H Braaten, H Lie, and MA Tognarelli. Experimental investigation of vortex-induced vibration of long marine risers. *Journal of fluids and structures*, 21(3):335–361, 2005.

[66] Mauricio C Vanzulli and Jorge M Pérez Zerpa. A consistent co-rotational formulation for aerodynamic nonlinear analysis of flexible frame structures. *arXiv preprint arXiv:2204.10545*, 2022.

[67] R. Violette, E. de Langre, and J. Szydlowski. Computation of vortex-induced vibrations of long structures using a wake oscillator model: Comparison with DNS and experiments. *Computers & Structures*, 85(11):1134–1141, June 2007. ISSN 0045-7949. doi: 10.1016/j.compstruc.2006.08.005. URL http://www.sciencedirect.com/science/article/pii/S004579490600229X.

[68] L Wang, TL Jiang, HL Dai, and Q Ni. Three-dimensional vortex-induced vibrations of supported pipes conveying fluid based on wake oscillator models. *Journal of Sound and Vibration*, 422:590–612, 2018.

[69] RHJ Willden and JMR Graham. Numerical prediction of viv on long flexible circular cylinders. *Journal of Fluids and Structures*, 15(3-4):659–669, 2001.

[70] Richard HJ Willden and J Michael R Graham. Multi-modal vortex-induced vibrations of a vertical riser pipe subject to a uniform current profile. *European Journal of Mechanics-B/Fluids*, 23(1):209–218, 2004.

[71] Yifan Xia, Sébastien Michelin, and Olivier Doaré. Fluid-solid-electric lock-in of energy-harvesting piezoelectric flags. *Physical review applied*, 3(1):014009, 2015.